Supporting Information for Monod-Wyman-Changeux Analysis of Ligand-Gated Ion Channel Mutants

Tal Einav[†] and Rob Phillips[*,‡]

[†]*Department of Physics, California Institute of Technology, Pasadena, California 91125, United States*

[‡]*Department of Applied Physics and Division of Biology and Biological Engineering, California Institute of Technology, Pasadena, California 91125, United States*

E-mail: phillips@pboc.caltech.edu

Phone: (626) 395-3374

A Additional Ion Channel Data

In this section, we explore some of the additional experimental measurements available for the nAChR and CNGA2 systems studied above and elaborate on several calculations mentioned in the text. In A.1, we analyze the time scale required for an ion channel to reach equilibrium. In A.2, we present data on additional L251S nAChR mutants. Using these mutants, we examine the approximation made in the text that only the *total* number of mutations, and not the identity of the subunits mutated, influences the resulting nAChR mutant behavior. In A.3, we examine $p_{\text{open}}(c)$ for the classes of ion channels considered in the text and comment on how this probability differs from the normalized current. In A.4, we examine data from a similar class of L251T mutations and show that their qualitative behavior is similar to the L251S mutants. In A.5, we discuss measurements of combinations of CNGA2 ion channels.

A.1 Dynamics Towards Equilibrium

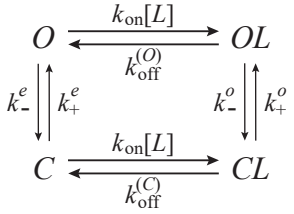

Figure S1: Rates for an ion channel with one ligand binding site. The ion channel tends to transition from the closed (C) state to the open (O) state after binding to ligand (L). We assume both ion channel states have the same diffusion-limited on-rate $k_{\text{on}} = 10^9 \frac{1}{\text{M}\cdot\text{s}}$. The remaining rates of the bound states should satisfy $k_{\text{off}}^{(C)} > k_{\text{off}}^{(O)}$ and $k_+^o > k_-^o$ so that ligand binding drives the ion channel to the open state OL.

In this section we derive an exact expression for the time constant for which an ion channel with one ligand binding site will come to equilibrium. This analysis can be readily extended numerically to include multiple ligand binding sites.

Fig S1 shows the rates between the four possible ion channel states: the unbound open (O) and closed (C) states as well as the bound open (OL) and closed (CL) states. We assume that there is a sufficient ligand $[L]$ in the system so that when the ligand binds to the ion channels its concentration does not appreciably diminish. Hence the rate equations for the system can be written in matrix form (with bold denoting vectors and matrices) as

$$\frac{d\boldsymbol{E}}{dt} = \boldsymbol{K}\boldsymbol{E} \tag{S1}$$

where the right hand side represents the product of the transition matrix

$$\boldsymbol{K} = \begin{pmatrix} -(k_+^e + k_{\text{on}}[L]) & k_{\text{off}}^{(C)} & k_-^e & 0 \\ k_{\text{on}}[L] & -(k_+^o + k_{\text{off}}^{(C)}) & 0 & k_-^o \\ k_+^e & 0 & -(k_-^e + k_{\text{on}}[L]) & k_{\text{off}}^{(O)} \\ 0 & k_+^o & k_{\text{on}}[L] & -(k_-^o + k_{\text{off}}^{(O)}) \end{pmatrix} \tag{S2}$$

and the vector representing the occupancy of each ion channel state

$$\boldsymbol{E} = \begin{pmatrix} [C] \\ [CL] \\ [O] \\ [OL] \end{pmatrix}. \tag{S3}$$

The matrix $\boldsymbol{K}$ can be decomposed as

$$\boldsymbol{K} = \boldsymbol{V}^{-1}\boldsymbol{\Lambda}\boldsymbol{V} \tag{S4}$$

where $\boldsymbol{V}$'s columns are the eigenvectors of $\boldsymbol{K}$ and $\boldsymbol{\Lambda}$ is a diagonal matrix whose entries are the eigenvalues of $\boldsymbol{K}$. In general, it is known that the eigenvalues of such a matrix $\boldsymbol{K}$ representing the dynamics of any graph such as Fig S1 has one eigenvalue that is 0 while the remaining eigenvalues are non-zero and have negative real parts.[1] (Indeed, because all of the columns of $\boldsymbol{K}$ add up to zero, $\boldsymbol{K}$ is not full rank and hence one of its eigenvalues must be zero.) Defining the vector

$$\tilde{\boldsymbol{E}} \equiv \boldsymbol{V}\boldsymbol{E} = \begin{pmatrix} \tilde{E}_1 \\ \tilde{E}_2 \\ \tilde{E}_3 \\ \tilde{E}_4 \end{pmatrix}, \tag{S5}$$

Eq (S1) can be rewritten as

$$\frac{d\tilde{\boldsymbol{E}}}{dt} = \boldsymbol{\Lambda}\tilde{\boldsymbol{E}}. \tag{S6}$$

If the eigenvalues of Λ are λ_1, λ_2, λ_3, and 0, then $\tilde{E}_j = c_j e^{\lambda_j t}$ for $j = 1, 2, 3$ and $\tilde{E}_4 = c_4$ where the c_j's are constants determined by initial conditions. Since the $\tilde{E}_j$'s are linear combinations of $[C]$, $[CS]$, $[O]$, and $[OS]$, this implies that the $-\frac{1}{\lambda_1}$,$-\frac{1}{\lambda_2}$, and $-\frac{1}{\lambda_3}$ (or $-\frac{1}{\Re(\lambda_j)}$ if the eigenvalues are complex) are the time scales for the normal modes of the system to come to equilibrium, with the largest value representing the time scale τ for the entire system to reach equilibrium,

$$\tau = \max\left(-\frac{1}{\lambda_1}, -\frac{1}{\lambda_2}, -\frac{1}{\lambda_3}\right). \tag{S7}$$

Although the eigenvalues of this matrix can be calculated in closed form, as roots of a cubic function, the full expression is complicated. Instead, we write the Taylor expansion of λ_1, λ_2, and λ_3 in the limit $k_+^o \to \infty$, since we suspect that the transition from $CS \to OS$ is extremely fast. In this limit, the λ_js take the forms

$$\lambda_1 = -(k_{\text{off}}^{(O)} + k_{\text{on}}[L]) + O\left(\frac{1}{k_+^o}\right) \tag{S8}$$

$$\lambda_2 = -(k_{\text{off}}^{(C)} + k_-^o + k_+^o) + O\left(\frac{1}{k_+^o}\right) \tag{S9}$$

$$\lambda_3 = -(k_{\text{on}}[L] + k_-^e + k_+^e) + O\left(\frac{1}{k_+^o}\right). \tag{S10}$$

Fig S2 shows an example of how the system attains its equilibrium starting from a random initial condition. The exact time scale Eq (S7) using the matrix eigenvalues leads to $\tau = 1.1 \times 10^{-3}\,\mathrm{s}$, which is very close to the approximation using Eqs (S8)-(S10) which yields $\tau^{(approx)} = 1.0 \times 10^{-3}\,\mathrm{s}$. The exact time scale is shown in Fig S2 as a dashed line, and states achieve near total equilibrium by $t = 10^{-2}\,\mathrm{s}$.

As a point of reference for this time scale described above for the system to come to equilibrium, there are two other relevant times scales for an ion channel: (1) the time scale for an ion channel to switch between the open and closed conformations and (2) the time scale for an ion channel to stay in its open conformation before switching to the closed conformation. The former occurs on the microsecond scale for nAChR,[2] while the latter occurs on the millisecond scale.[3,4] Thus, the time to transition between the closed and open conformations can be ignored, and the system reaches equilibrium after only a few transitions between the open and closed states.

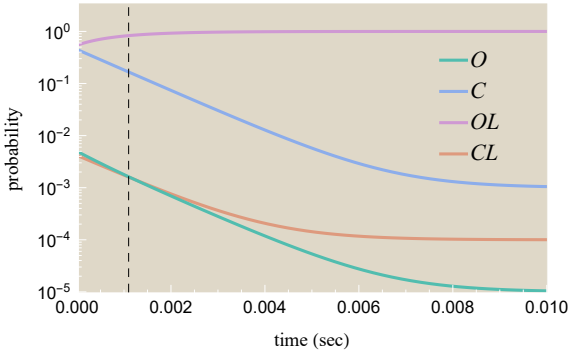

Figure S2: Kinetics of a system heading towards equilibrium. The relative probabilities of the four states are computed using Eqs (S1) and (S2) and the rate constants $k_{\mathrm{on}}[L] = 10^3 \frac{1}{\mathrm{s}}$, $k_{\mathrm{off}}^{(O)} = 10^{-2} \frac{1}{\mathrm{s}}$, $k_{\mathrm{off}}^{(C)} = 10^4 \frac{1}{\mathrm{s}}$, $k_+^o = 10^4 \frac{1}{\mathrm{s}}$, $k_-^o = 10 \frac{1}{\mathrm{s}}$, $k_+^e = 10 \frac{1}{\mathrm{s}}$, and $k_-^e = 10^3 \frac{1}{\mathrm{s}}$. Note that the rate constants must satisfy the cycle condition: the product of rates moving clockwise equals the product of rates going counterclockwise.[5] The dashed line indicates the exact time scale Eq (S7) for the system to reach equilibrium. Initial conditions were chosen randomly as $p_O = 0.005$, $p_C = 0.45$, $p_{OL} = 0.54$, and $p_{CL} = 0.005$.

Lastly, we compute the fractional occupancy of the four states ion channel states in steady state, $\frac{d\boldsymbol{E}}{dt} = \mathbf{0}$. We first make the standard assumption that the system is not expending energy to drive a cyclic flux in the system. Formally, this implies that the rate constants satisfy the cycle condition: the product of rates moving clockwise in Fig S1 equals the product of rates going counterclockwise,[5]

$$k_{\mathrm{on}}[L] k_-^o k_{\mathrm{off}}^{(C)} k_+^e = k_-^e k_{\mathrm{off}}^{(O)} k_{\mathrm{on}}[L] k_+^o. \tag{S11}$$

With this condition, the fractional occupancy of each state is given by

$$[C] = \frac{\frac{k_-^e}{k_+^e}}{\left(1+\frac{k_{\rm on}[L]}{k_{\rm off}^{(O)}}\right)+\frac{k_-^e}{k_+^e}\left(1+\frac{k_{\rm on}[L]}{k_{\rm off}^{(C)}}\right)} \tag{S12}$$

$$[CL] = \frac{\frac{k_-^e}{k_+^e}\frac{k_{\rm on}[L]}{k_{\rm off}^{(C)}}}{\left(1+\frac{k_{\rm on}[L]}{k_{\rm off}^{(O)}}\right)+\frac{k_-^e}{k_+^e}\left(1+\frac{k_{\rm on}[L]}{k_{\rm off}^{(C)}}\right)} \tag{S13}$$

$$[O] = \frac{1}{\left(1+\frac{k_{\rm on}[L]}{k_{\rm off}^{(O)}}\right)+\frac{k_-^e}{k_+^e}\left(1+\frac{k_{\rm on}[L]}{k_{\rm off}^{(C)}}\right)} \tag{S14}$$

$$[OL] = \frac{\frac{k_{\rm on}[L]}{k_{\rm off}^{(O)}}}{\left(1+\frac{k_{\rm on}[L]}{k_{\rm off}^{(O)}}\right)+\frac{k_-^e}{k_+^e}\left(1+\frac{k_{\rm on}[L]}{k_{\rm off}^{(C)}}\right)}, \tag{S15}$$

A system in steady state which satisfies the cycle condition must necessarily be in thermodynamic equilibrium,[6] which implies that these fractional occupancies must be identical to the result derived from the Boltzmann distribution (see Fig 2). And indeed, this correspondence is made explicit if we define

$$e^{-\beta\epsilon} = \frac{k_-^e}{k_+^e} \tag{S16}$$

$$K_{\rm O} = \frac{k_{\rm off}^{(O)}}{k_{\rm on}} \tag{S17}$$

$$K_{\rm C} = \frac{k_{\rm off}^{(C)}}{k_{\rm on}}. \tag{S18}$$

In this way, the MWC parameters can be defined through the ratios of the rate parameters of the system.

A.2 Additional nAChR Mutants

In addition to the five constructs shown in Fig 3, namely $n = 0$ (wild type), $n = 1$ ($\alpha_2\beta\gamma^*\delta$), $n = 2$ ($\alpha_2^*\beta\gamma\delta$), $n = 3$ ($\alpha_2\beta^*\gamma^*\delta^*$), and $n = 4$ ($\alpha_2^*\beta\gamma^*\delta^*$), Labarca *et al.* constructed multiple other ion channel mutants listed in Table S1.[3] While complete dose-response curves are not available for these other constructs, their $[EC_{50}]$ values were measured. Using the $K_{\rm O}$ and $K_{\rm C}$ values for this entire class of mutants given in Fig 3, we can use the $[EC_{50}]$ measurements to fit the $\beta\epsilon$ value of each mutant, thereby providing us with a complete description of each mutant.

In particular, we can predict the dose-response curves of each of these mutants, as shown in Fig S3. We overlay the data from Fig 3 on top of these theoretical curves, where mutants with the same total number n of mutations are drawn as shades of the same color. Note that

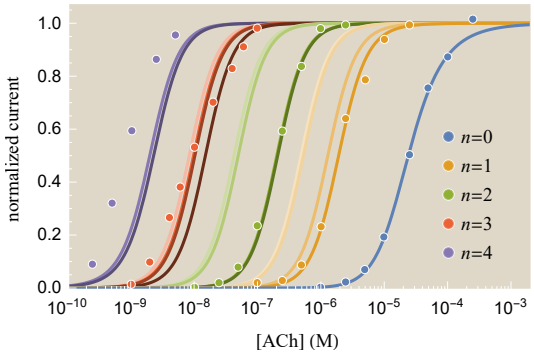

Figure S3: Categorizing the full set of ion channel mutants. Using the best-fit K_O and K_C values obtained from the five mutants in Fig 3, we can use the measured $[EC_{50}]$ value for each mutant in Table S1 to determine its $\beta\epsilon$ parameter. Thus, a single data point for each mutant enables us to predict its complete dose-response curve. All mutants with the same total number n of mutations are plotted in shades of the same color, together with the complete dose-response curves from Fig 3. Note that while each mutant family spans a range of $[EC_{50}]$ values, the classes are distinct and do not overlap.

there was some error in the original measurements, since the reported $[EC_{50}]$ value for the $n = 4$ ($\alpha_2^*\beta\gamma^*\delta^*$) mutant shown in purple dots in Fig S3 should clearly be less than 10^{-9} M, even though it was given as $(2.0 \pm 0.6) \times 10^{-9}$ M in Ref. 3.

Table S1: Dose-response relations for mouse muscle ACh receptors containing various numbers of mutated L251S subunits (n). Mutated subunits are indicated by an asterisk ($*$). Standard error of the mean for $[EC_{50}]$ was less than 10% of the mean, except where given. Responses for the $\alpha_2^*\beta^*\gamma^*\delta^*$ mutant were too small for reliable measurements. Reproduced from Ref. 3.

n	subunits	$[EC_{50}]$ (nM)
0	$\alpha_2\beta\gamma\delta$	24,010
1	$\alpha\alpha^*\beta\gamma\delta$	1,290
	$\alpha_2\beta^*\gamma\delta$	531
	$\alpha_2\beta\gamma^*\delta$	1,910
	$\alpha_2\beta\gamma\delta^*$	486
2	$\alpha_2^*\beta\gamma\delta$	202
	$\alpha_2\beta^*\gamma^*\delta$	49.7
	$\alpha_2\beta^*\gamma\delta^*$	208 ± 69
	$\alpha_2\beta\gamma^*\delta^*$	42.7
3	$\alpha_2^*\beta^*\gamma\delta$	10.3
	$\alpha_2^*\beta\gamma^*\delta$	15.1
	$\alpha_2^*\beta\gamma\delta^*$	8.4 ± 1.3
	$\alpha_2\beta^*\gamma^*\delta^*$	9.8 ± 1.3
4	$\alpha_2^*\beta^*\gamma\delta^*$	2.3
	$\alpha_2^*\beta\gamma^*\delta^*$	2.0 ± 0.6
5	$\alpha_2^*\beta^*\gamma^*\delta^*$	< 1

Fig S3 demonstrates that not all subunit mutations cause a tenfold decrease in $[EC_{50}]$, but rather that there is a small spread in $[EC_{50}]$ depending on precisely which subunit was mutated. This variation is not unreasonable given that $\alpha_2\beta\gamma\delta$ nAChR is a heteropentamer. Indeed, such subunit-dependent spreading in $[EC_{50}]$ values has also been seen in other heteromeric ion channels[7,8] but is absent within homomeric ion channels such as the CNGA2 ion channel explored in the text.[4]

To explore this subunit-dependent shift in the dose-response curves, we now relax the assumption that mutating any of the four nAChR subunits results in an identical increase of roughly 5 k_BT to the allosteric gating energy ϵ. Instead, we allow each type of subunit to shift ϵ by a different amount upon mutation. We begin by writing the ϵ parameter of wild type nAChR as

$$\epsilon_{\alpha_2\beta\gamma\delta} = 2\epsilon_\alpha + \epsilon_\beta + \epsilon_\gamma + \epsilon_\delta, \tag{S19}$$

where ϵ_j denotes the gating energy contribution from subunit j and we have assumed that the five subunits independently contribute to channel gating. Upon mutation, we define the free energy differences of each type of subunit as

$$\Delta\epsilon_\alpha \equiv \epsilon_{\alpha^*} - \epsilon_\alpha \tag{S20}$$
$$\Delta\epsilon_\beta \equiv \epsilon_{\beta^*} - \epsilon_\beta \tag{S21}$$
$$\Delta\epsilon_\gamma \equiv \epsilon_{\gamma^*} - \epsilon_\gamma \tag{S22}$$
$$\Delta\epsilon_\delta \equiv \epsilon_{\delta^*} - \epsilon_\delta, \tag{S23}$$

where ϵ_{j^*} denotes the gating energy from the mutated subunit j.

The allosteric energy of any nAChR mutant can be found using the wild type energy $\epsilon_{\alpha_2\beta\gamma\delta} = -23.7\ k_BT$ from the main text together with $\Delta\epsilon_\alpha$, $\Delta\epsilon_\beta$, $\Delta\epsilon_\delta$, and $\Delta\epsilon_\gamma$. For example, the gating energy of $\alpha_2\beta^*\gamma\delta$ is given by $\epsilon_{\alpha_2\beta^*\gamma\delta} = \epsilon_{\alpha_2\beta\gamma\delta} + \Delta\epsilon_\beta$ while that of $\alpha_2^*\beta\gamma\delta^*$ is given by $\epsilon_{\alpha_2^*\beta\gamma\delta^*} = \epsilon_{\alpha_2\beta\gamma\delta} + 2\Delta\epsilon_\alpha + \Delta\epsilon_\delta$.

Using the measured $[EC_{50}]$ values of all the mutants in Table S1, we can fit the four $\Delta\epsilon_j$'s to determine how the different subunits increase the ion channel gating energy upon mutation. We find the values $\Delta\epsilon_\alpha = 4.4\ k_BT$, $\Delta\epsilon_\beta = 5.3\ k_BT$, $\Delta\epsilon_\gamma = 5.4\ k_BT$, and $\Delta\epsilon_\delta = 5.2\ k_BT$, which show a small spread about the value of roughly 5 k_BT found in the text by assuming that all four $\Delta\epsilon_j$'s are identical. To show the goodness of fit, we can compare the $[EC_{50}]$ values from this model to the experimental measurements in Table S1, as shown in Fig S4.

A.3 $p_{\mathrm{open}}(c)$ Curves

Although the dose-response curves we analyze for nAChR were all presented using normalized current, the underlying physical process - namely, the opening and closing of the ion channel - is not required to go from 0 to 1. Fig S5 shows the normalized dose-response curves from Fig 3A together with the average probability that each ion channel mutant will be open, $p_{\mathrm{open}}(c)$. Note that these $p_{\mathrm{open}}(c)$ curves have exactly the same shape as the normalized current curves but are compressed in the vertical direction to have the leakiness and dynamic range specified by Fig 4A and B.

From the viewpoint of these $p_{\mathrm{open}}(c)$ curves, various nuances of this ion channel class

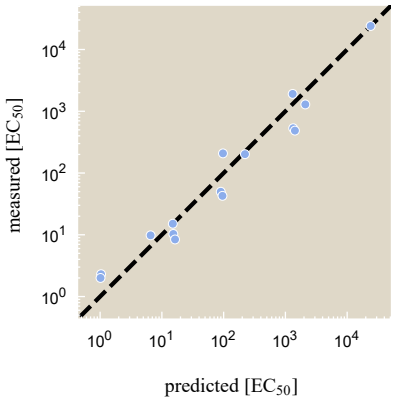

Figure S4: Mutating different nAChR subunits changes the gating energy ϵ by different amounts. Using a linear model where each subunit independently contributes to channel gating, we fit all of the $[EC_{50}]$ values in Table S1 to compute the increase of the gating energy ϵ when each subunit of $\alpha_2\beta\gamma\delta$ nAChR is mutated (see Eqs (S20)-(S23)). Upon mutation, a subunit of type j increases the gating energy by $\Delta\epsilon_j$, where $\Delta\epsilon_\alpha = 4.4\ k_BT$, $\Delta\epsilon_\beta = 5.3\ k_BT$, $\Delta\epsilon_\gamma = 5.4\ k_BT$, and $\Delta\epsilon_\delta = 5.2\ k_BT$. For each mutant in Table S1, the $[EC_{50}]$ from the model can be compared to the corresponding experimental measurement, with the black dashed line denoting the line of equality $y = x$.

stand out more starkly. For example, the four mutant channels have $p_{\text{open}}^{\text{max}} \approx 1$, noticeably larger than the $p_{\text{open}}^{\text{max}} \approx 0.9$ value of the wild type channel. In addition, the $n = 4$ mutant is the only ion channel with non-negligible leakiness, and Fig 4A suggests that an $n = 5$ mutant with all five subunits carrying the L251S mutation would have an even larger leakiness value greater than ½. In other words, the $n = 5$ ion channel is open more than half the time even in the absence of ligand, which could potentially cripple or kill the cell. This may explain why Labarca *et al.* made the $n = 5$ strain but were unable to measure its properties.[3]

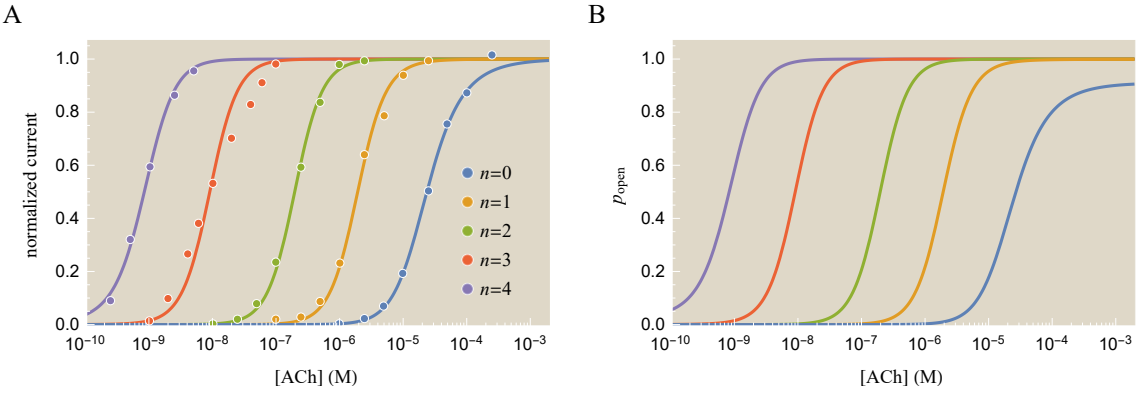

Figure S5: Probability that an nAChR mutant will be open. (A) Normalized current curves of the five nAChR mutants from Fig 3A. (B) The probability that each ion channel will be open is given by Eq (1). Note that the wild type ion channel has a smaller dynamic range and the $n = 4$ mutant has a noticeably larger leakiness than the other mutants.

Fig S6 repeats this same analysis for the CNGA2 dose-response curves from Fig 6A. In this case, all of the ion channel mutants have uniformly small values of $p_{\text{open}}^{\text{min}} \approx 0.03$ and

uniformly large $p_{\text{open}}^{\max} \approx 1$, as indicated by Fig 8A and B. Therefore, the $p_{\text{open}}(c)$ curves look very similar to the normalized currents.

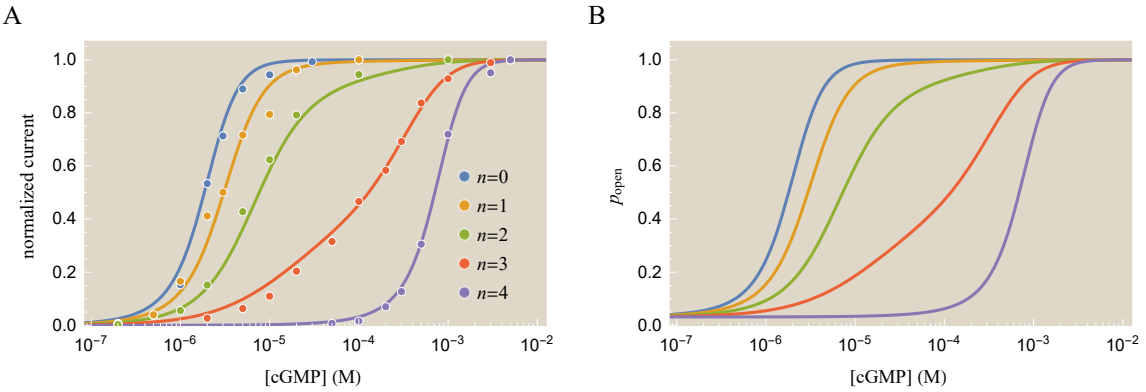

Figure S6: Probability that a CNGA2 mutant will be open. (A) CNGA2 dose-response curves from Fig 6A. (B) The probability that each ion channel will be open is given by Eq (1). Since all of the channels have small leakiness (≈ 0.03) and large dynamic range, the $p_{\text{open}}(c)$ curves are nearly identical to the normalized current curves.

A.4 nAChR L251T Mutation

In this section we consider a separate nAChR data from the one considered in the main paper. Filatov and White constructed nAChR ion channel mutants closely related to those of Labarca *et al.* but employing a L251T mutation.[9] They measured the $[EC_{50}]$ of multiple such constructs with the L251T mutation on different subsets of nAChR subunits, with the results shown in Fig S7A as a function of the total number of mutated subunits n.

As in the case of the L251S mutations from Labarca (see Fig S3 and Table S1), there was some variation in $[EC_{50}]$ between different mutants with the same total number of mutations n, but the entire class of mutants is well approximated as having $[EC_{50}]$ exponentially decrease with each additional mutation. Utilizing our analytical formula for the $[EC_{50}]$ of nAChR, Eq (11), and assuming that each mutation changes ϵ by a fixed amount $\Delta\epsilon$, the shift in $[EC_{50}]$ due to n mutations is given by

$$[EC_{50}] = e^{-\beta(\epsilon^{(0)}+n\Delta\epsilon)/2} K_{\text{O}}. \tag{S24}$$

We can fit the logarithm of the $[EC_{50}]$ values in Fig S7A to a linear function going through the wild type ($n = 0$) data point to obtain $\Delta\epsilon = 3.64\ k_{\text{B}}T$ from the slope of this line. This value is comparable to that found for the L251S mutation (where $\Delta\epsilon = 5\ k_{\text{B}}T$).

With the gating energy now fully determined for any number of mutations n, and using the K_{O} and K_{C} parameters from Fig 3, we now have a complete theoretical model of the L251T nAChR mutant class. For example, we can plot the predicted dose-response curves for all such mutants. Fig S7B shows these predictions together with experimentally measured responses from the wild type channel and three mutant constructs. The dose-response predictions should match the data on average for the entire class of mutants, although individual channel responses may be slightly off. For example, Fig S7A indicates that the $[EC_{50}]$

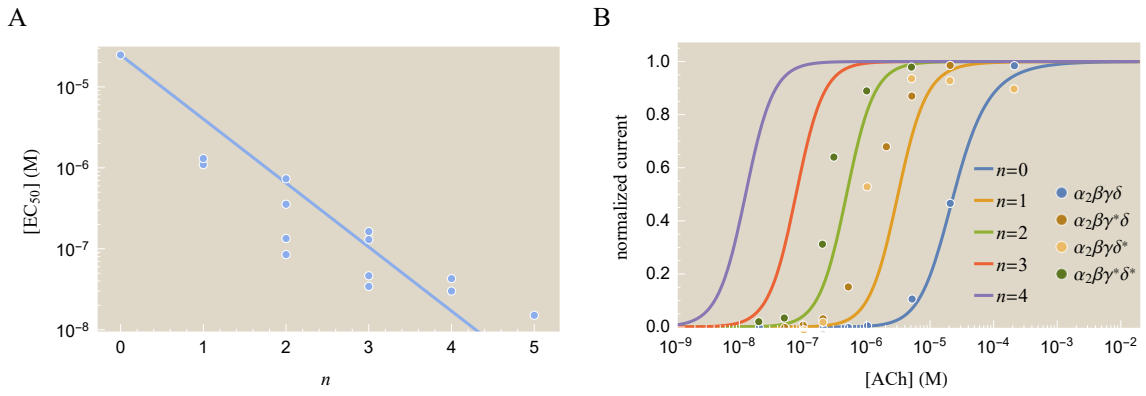

Figure S7: Effects of L251T mutations on nAChR. (A) $[EC_{50}]$ values for another class of L251T mutations introduced at different combinations of subunits.[9] This data set is separate from the L251S mutation considered in the main text. The $[EC_{50}]$ mainly depends on the total number of mutations, $[EC_{50}] \propto e^{-1.82n}$, although there is slight variation depending upon which subunits are mutated. From Eq (S24), we find that each mutation imparts $\Delta\epsilon = 3.64\ k_BT$. (B) Once the MWC parameters have been fixed from the $[EC_{50}]$ measurements, we can predict the full dose-response curves for the entire class of L251T nAChR mutants. Overlaid on these theoretical prediction are four experimentally measured response curves for the wild type ($\alpha_2\beta\gamma\delta$), two $n = 1$ single mutants ($\alpha_2\beta\gamma^*\delta$ and $\alpha_2\beta\gamma\delta^*$), and the $n = 2$ double mutant ($\alpha_2\beta\gamma^*\delta^*$). We expect the predicted dose-response curves to match the data on average for the entire class of mutants, but Part A shows that the $[EC_{50}]$ of the $n = 1$ and $n = 2$ mutants will be overestimated while that of the $n = 4$ and $n = 5$ mutants will be underestimated. Asterisks ($*$) in the legend denote L251T mutations.

of the $n = 1$ and $n = 2$ mutants will be lower than predicted while that of the $n = 4$ and $n = 5$ mutants (whose dose-response data was not provided) will be higher than predicted.

A.5 Combining Multiple Ion Channels

In this section, we consider the dose-response curve for the case in which the cell harbors both wild type and mutant ion channels. Given n_1 ion channels whose dose-response curves are governed by $p_{1,\text{open}}(c)$ and n_2 ion channels with a different response $p_{2,\text{open}}(c)$, the current produced by the combination of these two ion channels is given by

$$\text{current} \propto n_1 p_{1,\text{open}}(c) + n_2 p_{2,\text{open}}(c). \tag{S25}$$

Experimental measurements are computed on a relative scale so that the data runs from 0 to 1. Analytically, this amounts to subtracting the leakiness and dividing by the dynamic range,

$$(\text{normalized current})_{\text{tot}} = \frac{n_1 p_{1,\text{open}}(c) + n_2 p_{2,\text{open}}(c) - n_1 p_{1,\text{open}}^{\text{min}} - n_2 p_{2,\text{open}}^{\text{min}}}{n_1 p_{1,\text{open}}^{\text{max}} + n_2 p_{2,\text{open}}^{\text{max}} - n_1 p_{1,\text{open}}^{\text{min}} - n_2 p_{2,\text{open}}^{\text{min}}}. \tag{S26}$$

Wongsamitkul *et al.* constructed cells expressing both the $n = 0$ wild type ion channels and the $n = 4$ fully mutated ion channels in a ratio of 1:1 (i.e. $n_1 = n_2$) as shown in Fig S8.[4]

Recall from Fig 8 that these ion channels have very small leakiness ($p_{1,\text{open}}^{\text{min}} \approx p_{2,\text{open}}^{\text{min}} \approx$

0) and nearly full dynamic range ($p_{1,\text{open}}^{\max} \approx p_{2,\text{open}}^{\max} \approx 1$). This implies that $p_{1,\text{open}}(c) \approx$ (normalized current)$_1$ and $p_{2,\text{open}}(c) \approx$ (normalized current)$_2$, so that the total normalized current due to the combination of ion channels is given by

$$(\text{normalized current})_{\text{tot}} = \frac{(\text{normalized current})_1 + (\text{normalized current})_2}{2}. \tag{S27}$$

Fig S8 shows that this simple prediction compares well to the measured data.

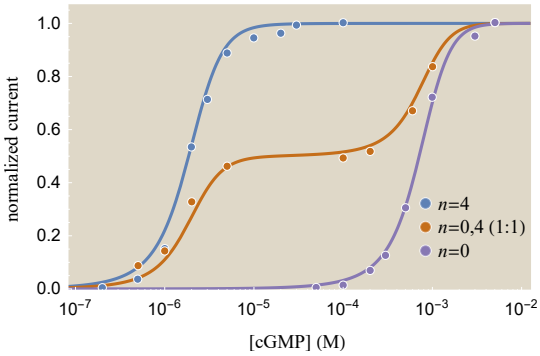

Figure S8: Normalized currents for combinations of CNGA2 ion channels. Channel currents of cells producing equal amounts of wild type $n = 0$ and the $n = 4$ mutant ion channels. As shown in Eq (S27), the resulting dose-response curve equals the average of the $n = 0$ and $n = 4$ individual response curves.

B Computing nAChR and CNGA2 Characteristics

In B.1, we derive Eqs (9)-(12), the approximations for the leakiness, dynamic range, $[EC_{50}]$, and the effective Hill coefficient h for the general MWC model Eq (1). We begin by Taylor expanding the well known exact expressions from Ref. 10 in the limit $1 \ll e^{-\beta\epsilon} \ll \left(\frac{K_C}{K_O}\right)^m$, which we found to be appropriate for both the nAChR and CNGA2 ion channels, and find the lowest order approximations.

Following that, in B.2 we consider how mutations in the ligand dissociation constants K_O and K_C affect these four properties. We show that ion channel dose-response curves are robust to changes in K_O and K_C aside from left-right shifts dictated by $[EC_{50}] = e^{-\beta\epsilon/m} K_O$. This discussion complements the nAChR section of the text where we considered mutations of the $\beta\epsilon$ parameter.

Lastly, in B.3 we determine how ion channels comprised of a mix of wild type subunits (with ligand dissociation constants K_O and K_C) and mutant subunits (with dissociation constants K_O^* and K_C^*) influences the four properties. Specifically, we focus on the analytically tractable case where half of the subunits are wild type and the other half are mutated (see Eqs (18) and (19) in the text).

B.1 Characteristics of the MWC Model

Using $1 \ll e^{-\beta\epsilon}$, the leakiness Eq (5) can be expanded as

$$\text{leakiness} = \frac{1}{1+e^{-\beta\epsilon}} \approx e^{\beta\epsilon}. \tag{S28}$$

Therefore, ion channels have a very small leakiness which scales exponentially with $\beta\epsilon$. Fig S9A shows that this is a good approximation across the entire range of parameters within the class of nAChR mutants, $-24 \leq \beta\epsilon \leq -4$.

The dynamic range Eq (6) can be similarly expanded to obtain

$$\text{dynamic range} = \frac{1}{1+e^{-\beta\epsilon}\left(\frac{K_O}{K_C}\right)^m} - \frac{1}{1+e^{-\beta\epsilon}} \approx 1 - e^{-\beta\epsilon}\left(\frac{K_O}{K_C}\right)^m - e^{\beta\epsilon}. \tag{S29}$$

Keeping only the lowest order term yields the approximation Eq (10) that ion channels have full dynamic range. Fig S9B shows that keeping the first order terms in Eq (S29) also captures the behavior of the wild type channel ($\beta\epsilon^{(0)} = -23.7$) and the $n = 4$ mutant ($\beta\epsilon^{(4)} = -4.0$).

We next turn to the $[EC_{50}]$ Eq (7), whose exact analytic formula is given by[11]

$$[EC_{50}] = K_O \frac{1-\lambda^{\frac{1}{m}}}{\lambda^{\frac{1}{m}} - \frac{K_O}{K_C}} \tag{S30}$$

where

$$\lambda = \frac{2 - \left(p_{\text{open}}^{\min} + p_{\text{open}}^{\max}\right)}{e^{-\beta\epsilon}\left(p_{\text{open}}^{\min} + p_{\text{open}}^{\max}\right)}. \tag{S31}$$

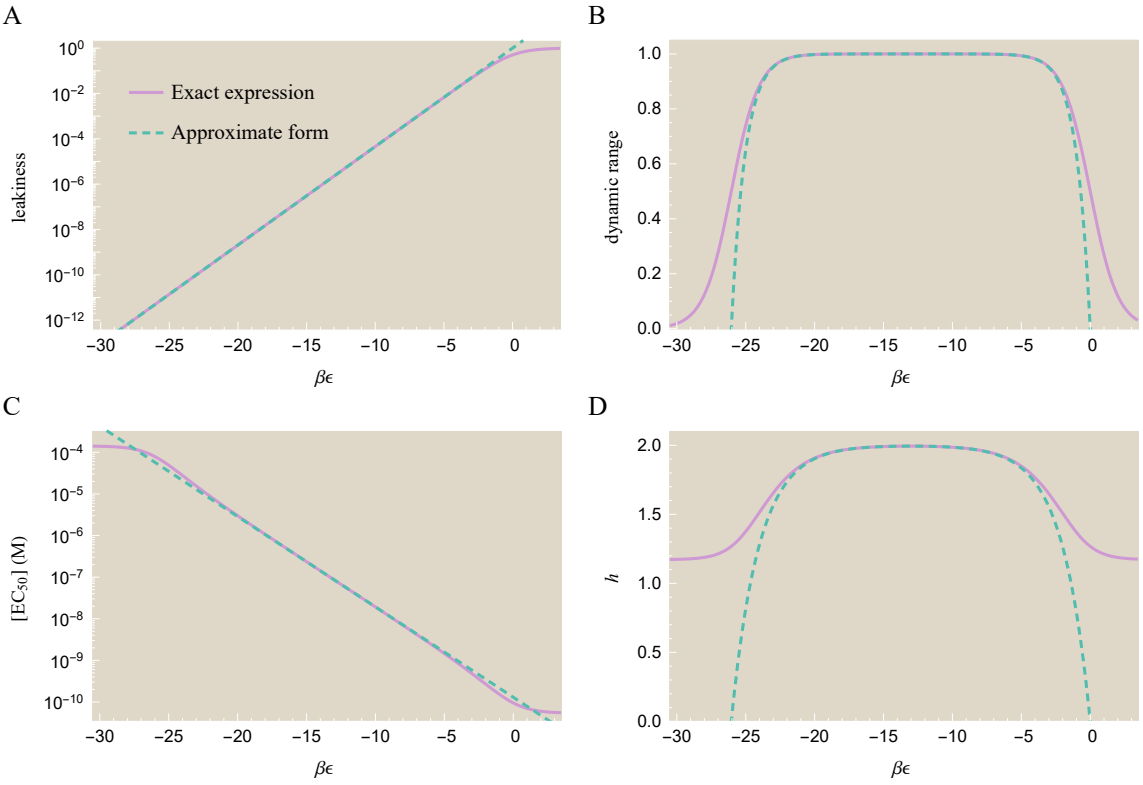

Figure S9: Exact and approximate expressions for nAChR characteristics. The approximations Eqs (S28)-(S34) (dashed, teal) are valid in the limit $1 \ll e^{-\beta\epsilon} \ll \left(\frac{K_C}{K_O}\right)^m$ where they closely match the exact expressions (purple). (A) Leakiness can be approximated as an exponentially increasing function of $\beta\epsilon$. (B) To lowest order, the dynamic range of an ion channel should approach unity, with deviations only at very large and very small $\beta\epsilon$ values. (C) The $[EC_{50}]$ is an exponentially decreasing function of $\beta\epsilon$. (D) The effective Hill coefficient is roughly constant for all mutants, but as with the dynamic range it decreases for very large and very small $\beta\epsilon$ values.

The limit $1 \ll e^{-\beta\epsilon} \ll \left(\frac{K_C}{K_O}\right)^m$ suggests that we Taylor expand this formula to lowest order about $e^{-\beta\epsilon}\left(\frac{K_O}{K_C}\right)^m \approx 0$ and $e^{-\beta\epsilon} \approx \infty$, which yields

$$\begin{aligned}
[EC_{50}] &\approx K_O \frac{\frac{K_C}{K_O}\left(\left(1-\frac{1}{2+e^{-\beta\epsilon}}\right)^{1/m}\right)}{\frac{K_C}{K_O}\left(\frac{1}{2+e^{-\beta\epsilon}}\right)^{1/m}-1} \\
&\approx K_O \frac{\frac{K_C}{K_O}\left(1-e^{\beta\epsilon/m}\right)}{\frac{K_C}{K_O}e^{\beta\epsilon/m}-1} \\
&\approx K_O \frac{\frac{K_C}{K_O}}{\frac{K_C}{K_O}e^{\beta\epsilon/m}} \\
&= K_O e^{-\beta\epsilon/m}.
\end{aligned} \tag{S32}$$

Thus, the $[EC_{50}]$ decreases exponentially with ϵ, although this effect is diminished with the number of ligand binding sites m. The precise relationship $[EC_{50}] \propto e^{-\beta\epsilon/2}$ for the nAChR data is shown in Fig S9C.

Finally, we turn to the effective Hill coefficient, whose exact analytic form is given by[11]

$$h = \frac{m[EC_{50}]\,(K_C - K_O)\left(p_{\text{open}}^{\min} + p_{\text{open}}^{\max}\right)\left(2 - p_{\text{open}}^{\min} - p_{\text{open}}^{\max}\right)}{\left(p_{\text{open}}^{\min} - p_{\text{open}}^{\max}\right)\left([EC_{50}] + K_O\right)\left([EC_{50}] + K_C\right)}, \tag{S33}$$

where we have used $p_{\text{open}}^{\min}$ and $p_{\text{open}}^{\max}$ from Eqs (3) and (4) as well as the $[EC_{50}]$ formula Eq (S30). Again, we make a Taylor series of this expression about $e^{-\beta\epsilon}\left(\frac{K_O}{K_C}\right)^m \approx 0$ and $e^{-\beta\epsilon} \approx \infty$ to obtain the lowest order approximation, which is given by

$$\begin{aligned} h &\approx m\frac{\frac{K_C}{K_O}+1}{\frac{K_C}{K_O}-1} - m\frac{\left(\frac{1}{2+e^{-\beta\epsilon}}\right)^{-1/m}}{\frac{K_C}{K_O}-1} - m\frac{\frac{K_C}{K_O}\left(\frac{1}{2+e^{-\beta\epsilon}}\right)^{1/m}}{\frac{K_C}{K_O}-1} - 2me^{\beta\epsilon}\frac{\frac{K_C}{K_O}\left(\frac{1}{2+e^{-\beta\epsilon}}\right)^{1/m}}{\frac{K_C}{K_O}-1} \\ &\approx m - m\frac{e^{-\beta\epsilon/m}}{\frac{K_C}{K_O}} - m\frac{\frac{K_C}{K_O}e^{\beta\epsilon/m}}{\frac{K_C}{K_O}} - 2me^{\beta\epsilon}\frac{\frac{K_C}{K_O}e^{\beta\epsilon/m}}{\frac{K_C}{K_O}} \\ &\approx m - m\frac{K_O}{K_C}e^{-\beta\epsilon/m} - me^{\beta\epsilon/m}. \end{aligned} \tag{S34}$$

Note that in the second step, we used the stronger constraint that $\frac{K_C}{K_O} \gg 1$, although it is still reasonably satisfied for both the nAChR ($\frac{K_C}{K_O} = 6 \times 10^5$) and CNGA2 ($\frac{K_C}{K_O} = 17$) ion channels considered in the text. By keeping the lowest order term, we recoup Eq (12) that all ion channels have the same sharp response, and that this sharpness increases linearly with the number of ligand binding sites. Fig S9D shows that by keeping the first order terms in Eq (S34), the shallower responses of the wild type ($\beta\epsilon^{(0)} = -23.7$) and $n = 4$ mutant ($\beta\epsilon^{(4)} = -4.0$) can also be well approximated.

B.2 Mutations Affecting the Ligand-Channel Dissociation Constants

In this section, we discuss how the leakiness, dynamic range, $[EC_{50}]$, and effective Hill coefficient h vary when the channel-ligand dissociation constants K_O and K_C are perturbed, as can be accomplished by mutating the ligand binding domain. Recall that ligand-gated ion channels are typically closed in the absence of ligand ($\epsilon < 0$) and open when bound to ligand ($K_O < K_C$).

Fig S10 shows the four ion channel properties using the parameters of the wild type CNGA2 ion channel ($\beta\epsilon = -3.4$ and $m = 4$ ligand binding sites) and letting the ratio $\frac{K_O}{K_C}$ of dissociation constants vary. All four graphs demonstrate that the ion channel's traits are nearly insensitive to changes in the dissociation constants provided that K_O does not approach K_C. In the limit $K_O \to K_C$, the ligand no longer drives the ion channel to open, causing the dynamic range to shrink to zero. As such, the behavior of the $[EC_{50}]$ and h in this limit should be considered as artifacts from taking this limit (since neither trait is well defined when the dynamic range shrinks to zero). For reference, the wild type CNGA2

channel has $\frac{K_O}{K_C} = 0.06$.

Note that the y-axis in Fig S10C plots $\frac{[EC_{50}]}{K_O}$, so if both K_O and K_C are reduced by a constant factor, then the $[EC_{50}]$ will also be reduced by this same factor. In the limit $\frac{K_O}{K_C} \to 0$, $[EC_{50}] = K_O \left(2 + e^{-\beta\epsilon}\right)^{1/m} - 1 \approx 1.4 K_O$ for the wild type CNGA2 channel (see Eq (S30)).

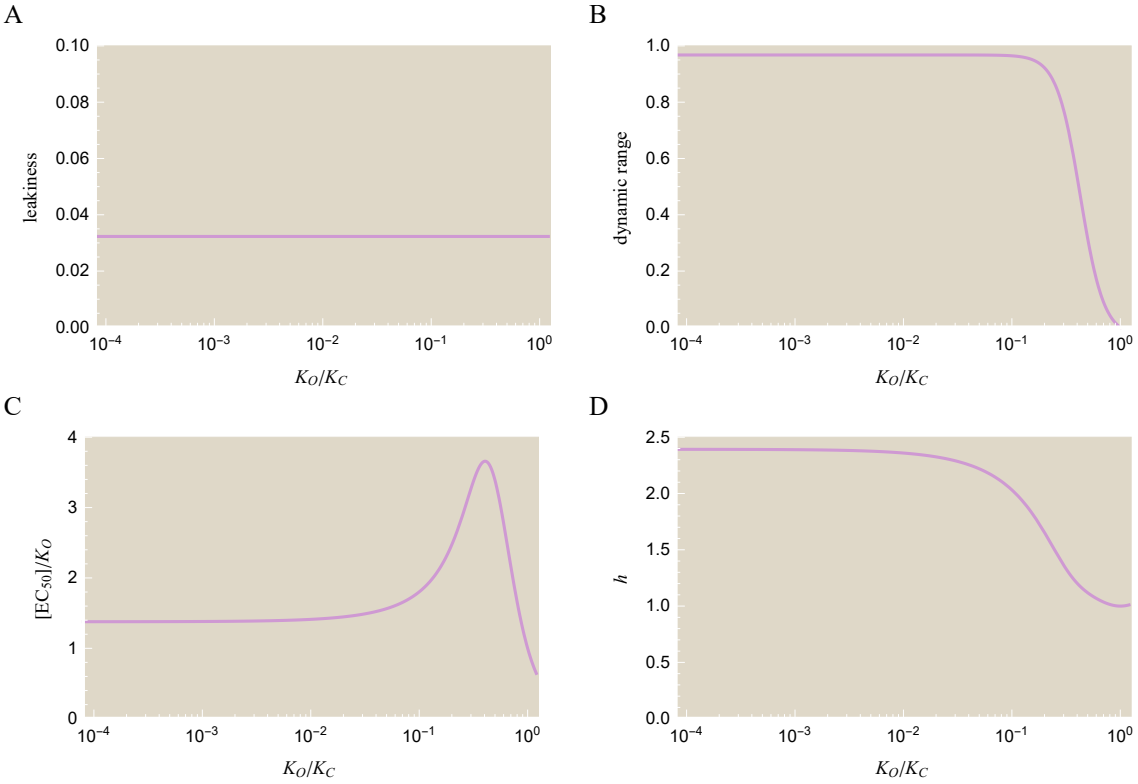

Figure S10: CNGA2 properties are robust to changes in the ligand dissociation constants. (A) The leakiness does not depend on either dissociation constant. (B) The dynamic range is near unity for set of dissociation constants where $\frac{K_O}{K_C} \leq 0.1$, as was found for both the nAChR and CNGA2 systems. For larger ratios of the dissociation constants, the ligand no longer drives the ion channel to open. (C) When $\frac{K_O}{K_C} \leq 0.1$, $[EC_{50}] \approx 1.4 K_O$ is proportional to K_O but robust to the ratio of dissociation constants. (D) The effective Hill coefficient is also robust to changes in the dissociation constants, with $h \approx 2.4$ when $\frac{K_O}{K_C} \leq 0.1$.

B.3 The Heterooligomeric CNGA2 Channel

We now consider an ion channel with m subunits, each of which could either be a wild type subunit (with dissociation constants K_O and K_C) or a mutated subunit (with dissociation constants K_O^* and K_C^*). Each subunit contains a single ligand binding site. We compute the leakiness, dynamic range, $[EC_{50}]$, and the effective Hill coefficient h of an ion channel composed of n mutated subunits and $m - n$ wild type subunits. In the text, we analyzed the specific case of the CNGA2 ion channel with $m = 4$ subunits.

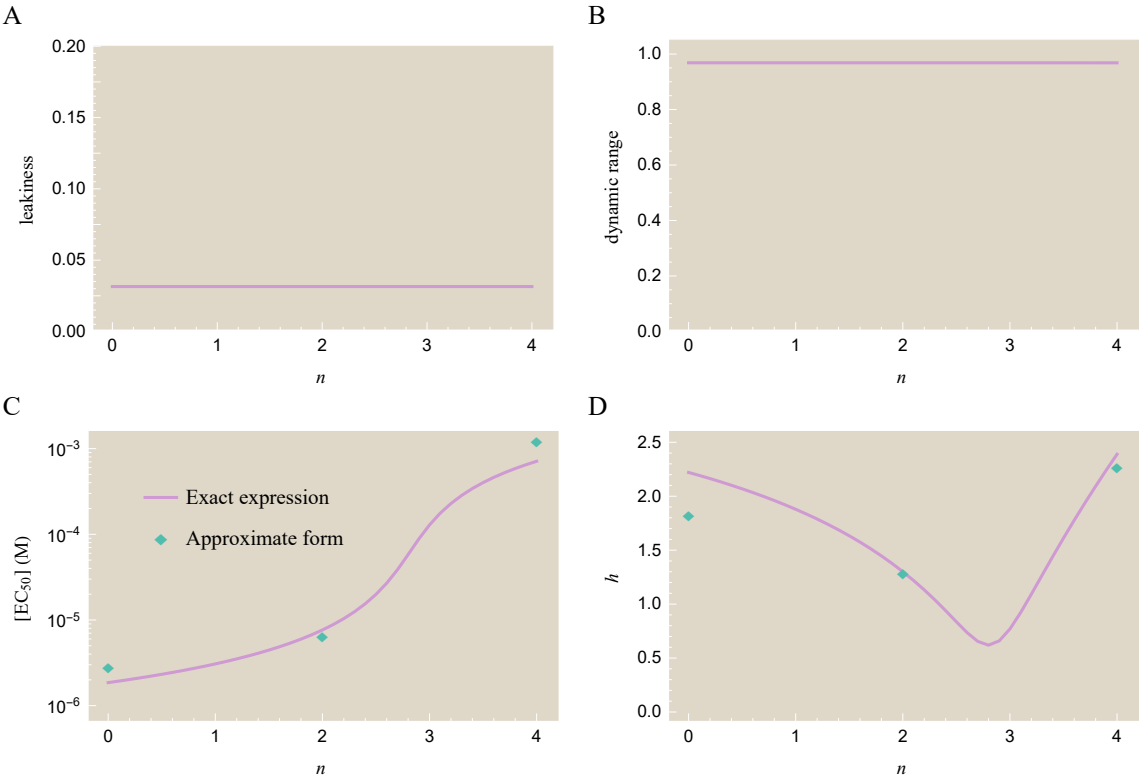

Figure S11: Effects of mixing two types of subunits in the CNGA2 ion channel. The CNGA2 ion channel is composed of $m = 4$ subunits, each of which has one ligand binding site. n of these subunits are mutated so as to have weaker ligand binding affinity. (A) The leakiness of the CNGA2 ion channel Eq (S37) is uniformly small. (B) All of the mutants have nearly full dynamic range Eq (S38) because the open channel dissociations constants ($K_{\rm O}$ and $K^*_{\rm O}$) are significantly larger than the closed channel dissociation constants ($K_{\rm C}$ and $K^*_{\rm C}$). (C) The exact expression (solid, purple) for the $[EC_{50}]$ is shown along with approximations for the $n = 0$, 2, and 4 ion channels (teal diamonds) from Eqs (S32) and (S48). Because the mutated subunits bind poorly to ligand, the $[EC_{50}]$ increases with n. (D) The effective Hill coefficient Eqs (S34) and (S50) can be approximated in the same manner as the $[EC_{50}]$. Although the homooligomeric $n = 0$ and $n = 4$ channels have sharp responses, the effect of combining both types of subunits ($n = 1$, 2, and 3) leads to a flatter response.

We begin by taking the limits of $p_{\rm open}(c)$, Eq (15), in the absence of ligand, which is given by

$$p_{\rm open}^{\rm min} = \frac{1}{1 + e^{-\beta\epsilon}}, \tag{S35}$$

and in the presence of saturating levels of ligand, which is given as

$$p_{\rm open}^{\rm max} = \frac{1}{1 + e^{-\beta\epsilon}\left(\frac{K_{\rm O}}{K_{\rm C}}\right)^{m-n}\left(\frac{K^*_{\rm O}}{K^*_{\rm C}}\right)^{n}}. \tag{S36}$$

Throughout this analysis, we assume $K_{\rm O} < K_{\rm C}$ and $K^*_{\rm O} < K^*_{\rm C}$ so that ligand binding makes both the wild type and mutant subunits more likely to open.

The two limits of $p_{\text{open}}(c)$ above allow us to directly compute the leakiness and dynamic range of the ion channels. The former is given by

$$\text{leakiness} = \frac{1}{1+e^{-\beta\epsilon}}, \tag{S37}$$

which has an identical form to the leakiness of the MWC model Eq (S28). As shown in Fig S11A, the leakiness does not depend explicitly on the number of mutated subunits n. We next turn to the formula for the dynamic range,

$$\text{dynamic range} = \frac{1}{1+e^{-\beta\epsilon}\left(\frac{K_{\text{O}}}{K_{\text{C}}}\right)^{m-n}\left(\frac{K^*_{\text{O}}}{K^*_{\text{C}}}\right)^{n}} - \frac{1}{1+e^{-\beta\epsilon}}. \tag{S38}$$

The first term in the dynamic range is approximately 1 because the open state affinities are always smaller than the closed state affinities by at least a factor of ten, and these factors are collectively raised to the m^{th} power. Since these ion channels also exhibit small leakiness, they each have a large dynamic range as shown in Fig S11B.

We next consider approximations for the $[EC_{50}]$ and effective Hill coefficient h. The wild type CNGA2 channel ($n = 0$) will necessarily follow the formulas derived above for the MWC model (Eqs (S32) and (S34)). Similarly, the homooligomeric CNGA2 ion channel comprised of all mutated subunits ($n = m$) will have the same formulas as the wild type channel but with $K_{\text{O}} \to K^*_{\text{O}}$ and $K_{\text{C}} \to K^*_{\text{C}}$.

To gain a sense of how the $[EC_{50}]$ and h vary for channels comprised of a mix of wild type and mutant subunits ($1 \leq n \leq m-1$), we analyze the $n = m/2$ case (implicitly assuming that m is even) where half the subunits are wild type and the other half are mutated. We begin with the $[EC_{50}]$ formula which by definition is given by

$$\frac{\left[\left(1+\frac{c}{K_{\text{O}}}\right)\left(1+\frac{c}{K^*_{\text{O}}}\right)\right]^{m/2}}{\left[\left(1+\frac{c}{K_{\text{O}}}\right)\left(1+\frac{c}{K^*_{\text{O}}}\right)\right]^{m/2} + e^{-\beta\epsilon}\left[\left(1+\frac{c}{K_{\text{C}}}\right)\left(1+\frac{c}{K^*_{\text{C}}}\right)\right]^{m/2}} = \frac{1}{2}\left(p^{\text{min}}_{\text{open}} + p^{\text{max}}_{\text{open}}\right). \tag{S39}$$

Rearranging the terms, we find

$$\lambda\left[\left(1+\frac{c}{K_{\text{O}}}\right)\left(1+\frac{c}{K^*_{\text{O}}}\right)\right]^{m/2} = \left[\left(1+\frac{c}{K_{\text{C}}}\right)\left(1+\frac{c}{K^*_{\text{C}}}\right)\right]^{m/2}, \tag{S40}$$

where we have introduced the same (positive) constant λ in Eq (S31) from the $[EC_{50}]$ of the standard MWC model,

$$\lambda = \frac{2 - \left(p^{\text{min}}_{\text{open}} + p^{\text{max}}_{\text{open}}\right)}{e^{-\beta\epsilon}\left(p^{\text{min}}_{\text{open}} + p^{\text{max}}_{\text{open}}\right)}. \tag{S41}$$

Upon raising both sides of Eq (S39) to the $\frac{2}{m}$ power, we find the quadratic equation

$$Ac^2 + Bc + C = 0 \tag{S42}$$

where

$$A = \frac{\lambda^{2/m}}{K_{\rm O} K_{\rm O}^*} - \frac{1}{K_{\rm C} K_{\rm C}^*} \tag{S43}$$

$$B = \frac{\lambda^{2/m}}{K_{\rm O}} + \frac{\lambda^{2/m}}{K_{\rm O}^*} - \frac{1}{K_{\rm C}} - \frac{1}{K_{\rm C}^*} \tag{S44}$$

$$C = \lambda^{2/m} - 1, \tag{S45}$$

which has the exact solution

$$[EC_{50}] = \frac{-B + \sqrt{B^2 - 4AC}}{2A}. \tag{S46}$$

To simplify this expression, we note that $|4AC|$ is smaller than B^2 by more than a factor of 10 for the CNGA2 parameter values, so that the square root can be approximated as $\sqrt{B^2 - 4AC} \approx B - \frac{2AC}{B}$, and hence the $[EC_{50}]$ becomes

$$[EC_{50}] \approx -\frac{C}{B} = \frac{1 - \lambda^{2/m}}{\frac{\lambda^{2/m}}{K_{\rm O}} + \frac{\lambda^{2/m}}{K_{\rm O}^*} - \frac{1}{K_{\rm C}} - \frac{1}{K_{\rm C}^*}}. \tag{S47}$$

To further simplify this result, we utilize the relationships $1 \ll e^{-\beta\epsilon} \ll \left(\frac{K_{\rm C}}{K_{\rm O}}\right)^{m/2}$ and $1 \ll e^{-\beta\epsilon} \ll \left(\frac{K_{\rm C}^*}{K_{\rm O}^*}\right)^{m/2}$ which hold for the CNGA2 parameters. In this limit, $p_{\rm open}^{\rm min} \approx 0$, $p_{\rm open}^{\rm max} \approx 1$, and $\lambda \approx e^{\beta\epsilon} \ll 1$, so that the formula for the $[EC_{50}]$ becomes

$$\begin{aligned}
[EC_{50}] &\approx \frac{1}{\frac{e^{2\beta\epsilon/m}}{K_{\rm O}} + \frac{e^{2\beta\epsilon/m}}{K_{\rm O}^*} - \frac{1}{K_{\rm C}} - \frac{1}{K_{\rm C}^*}} \\
&\approx \frac{1}{\frac{e^{2\beta\epsilon/m}}{K_{\rm O}} + \frac{e^{2\beta\epsilon/m}}{K_{\rm O}^*}} \\
&= e^{-2\beta\epsilon/m} \frac{K_{\rm O} K_{\rm O}^*}{K_{\rm O} + K_{\rm O}^*}.
\end{aligned} \tag{S48}$$

Since the mutated CNGA2 subunits have significantly weaker binding affinity ($K_{\rm O} \ll K_{\rm O}^*$), $[EC_{50}] \approx e^{-2\beta\epsilon/m} K_{\rm O}$ where the exponent is twice as large as the homooligomeric case Eq (S32). Fig S11C shows how the $[EC_{50}]$ gradually increases as more of mutant subunits are introduced into the ion channel, with the approximation for the $n = \frac{m}{2}$ mutant given by Eq (S48) while the $n = 0$ and $n = m$ mutants are described by Eq (S32).

We next turn to the effective Hill coefficient h. To greatly simplify the computation, we ignore all of the dissociation constants ($K_{\rm C} = 20 \times 10^{-6}$ M, $K_{\rm O}^* = 500 \times 10^{-6}$ M, and $K_{\rm C}^* = 140 \times 10^{-3}$ M) greater than the $[EC_{50}] \approx 6 \times 10^{-6}$ M, since they all enter $p_{\rm open}(c)$ as

$\left(1+\frac{c}{K_j}\right)^{m/2}$ with $m=4$ for CNGA2. Thus, the probability of the channel opening becomes

$$p_{\rm open}(c) \approx \frac{\left(1+\frac{c}{K_{\rm O}}\right)^{m/2}}{\left(1+\frac{c}{K_{\rm O}}\right)^{m/2}+e^{-\beta\epsilon}} \tag{S49}$$

where only the effect of the smallest dissociation constant ($K_{\rm O}=1.2\times10^{-6}$ M) is considered. Noting that $K_{\rm O}\ll K_{\rm O}^*$, the effective Hill coefficient is given by

$$\begin{aligned} h &\approx \frac{m}{(1+e^{2\beta\epsilon/m})\left(1+(1+e^{2\beta\epsilon/m})^{m/2}\right)} \\ &\approx \frac{m}{2}-\frac{m}{2}\left(\frac{m}{4}+1\right)e^{2\beta\epsilon/m}, \end{aligned} \tag{S50}$$

where in the second step we used the Taylor expansion about $e^{2\beta\epsilon/m}\ll 1$. Fig S11D shows the effective Hill coefficient together with the approximations for the homooligomeric ($n=0$ and $n=4$) ion channel Eq (S34) and the $n=2$ channel given by Eq (S50). As discussed in the text, the effective Hill coefficient exhibits a surprising decrease for ion channels comprised of a mix of both types of subunits ($1\le n\le 3$). Qualitatively, this comes about because the subunits of the $n=0$ wild type channel become sensitive to ligand at concentrations approaching $[EC_{50}]^{(n=0)}\approx e^{-\beta\epsilon/m}K_{\rm O}$ while the mutant subunits respond at the much larger concentrations $[EC_{50}]^{(n=4)}\approx e^{-\beta\epsilon/m}K_{\rm O}^*$. Channels containing both subunits consequently have a much flatter response over the range between $e^{-\beta\epsilon/m}K_{\rm O}$ and $e^{-\beta\epsilon/m}K_{\rm O}^*$.

C Data Fitting

In this section, we discuss the fitting procedure used on the nAChR and CNGA2 data sets. All fitting was done using nonlinear regression (NonlinearModelFit in *Mathematica*). A wide array of initial conditions were considered (for example, dissociation constants were sampled in the range $K_D \in [10^{-12}\text{ M}, 10^{0}\text{ M}]$ and allosteric energies were sampled across $\beta\epsilon \in [-30, 5]$), and the best-fit parameters were chosen from the fit with the largest coefficient of determination R^2. Because all dissociation constants are necessarily positive, we employed the standard trick of fitting the logarithms of dissociation constants, which improves both the fit stability and accuracy.

In C.1, we give more details on the fitting procedure. In C.2, we focus on the related point of the sensitivity of the MWC model parameter values. We compare experimentally measured values from the literature and analyze them in the context of the nAChR and CNGA2 data sets to determine how much flexibility the MWC model has in its ability to capture observed trends. In C.3, we discuss how values such as the $[EC_{50}]$ and effective Hill coefficient can be extracted from experimental measurements.

Lastly, in C.4 we discuss a critical issue for extracting best-fit parameters from data, namely, that multiple sets of parameters may exist which characterize the data nearly identically. This attribute of models, sometimes dubbed "sloppiness," can even exist in the MWC model we have developed for ion channels where there are only three parameters,[12] and it has also been found in an MWC model of hemoglobin.[13] We examine our results in light of this degeneracy.

C.1 Fitting Procedure

The fit parameters from Fig 3 are shown in Table S2. If the data is fit to the MWC model (Eqs (1) and (2)) with no constraints, then all of the degenerate parameter sets in Fig 10A would yield equally good fits. For example, any set of degenerate parameters with $K_{\text{O}} \leq 10^{-10}$ M have coefficient of determination $R^2 = 0.995 \pm 0.0002$. In other words, it is impossible to distinguish the actual set of parameter values for nAChR without further information. As highlighted in the main text, one method for lifting this degeneracy is to independently measure one model parameter, which could then be used to fix the remaining parameters. For example, measuring the leakiness of one of the nAChR mutants would fix its corresponding $\beta\epsilon^{(n)}$ parameter, resolving the degeneracy in Fig 10A. The leakiness of the $n = 3$ and $n = 4$ mutants is significantly larger than that of wild type nAChR, and hence should be possible to directly measure experimentally.

Next, we examine how much sloppiness would remain in the system if an experimental measurement fixed one of the $\beta\epsilon$ parameters. To do this, we arbitrarily choose $\beta\epsilon^{(4)} = -4.0$, and we then fit the remaining parameters with this constraint. With the degeneracy now removed from the model, Table S2 presents the mean parameter values and the error based on confidence intervals. Note that the remaining MWC parameters are all tightly constrained about their best-fit values, so that there is very little sloppiness left in the system after one parameter value is determined.

A similar fit procedure was used for the CNGA2 data set in Fig 6. Here, we arbitrarily fixed the parameter $K_{\text{C}}^{*} = 140 \times 10^{-3}$ M and fit the remaining parameters, with the results

Table S2: Best-fit parameters for the nAChR mutants given the constraint $\beta\epsilon^{(4)} = -4.0$. With this single parameter fixed, the remaining parameters have small uncertainties. R^2 represents the coefficient of determination.

K_O (M)	K_C (M)	$\beta\epsilon^{(0)}$	$\beta\epsilon^{(1)}$	$\beta\epsilon^{(2)}$	$\beta\epsilon^{(3)}$	$\beta\epsilon^{(4)}$	R^2
$(0.13 \pm 0.16) \times 10^{-9}$	$(11 \pm 7) \times 10^{-6}$	-23.7 ± 5.9	-19.2 ± 2.5	-14.6 ± 2.5	-8.5 ± 2.3	-4.0	0.995

Table S3: Best-fit parameters for the CNGA2 mutants with the constraint $K_C^* = 140 \times 10^{-3}$ M. As in the case of nAChR, we find that once one of the parameters has a fixed value, the degeneracy within the model is lifted and the remaining parameters have small uncertainties.

K_O (M)	K_C (M)	K_O^* (M)	K_C^* (M)	$\beta\epsilon$	R^2
$(1.2 \pm 0.1) \times 10^{-6}$	$(20 \pm 3) \times 10^{-6}$	$(500 \pm 100) \times 10^{-6}$	140×10^{-3}	-3.4 ± 0.2	0.997

shown in Table S3. Again, we find that with one parameter fixed, the remaining parameters are tightly constrained.

C.2 Comparison with Parameters Values from the Literature

In this section, we explore the degree of consistency between multiple independent measurements of the thermodynamic parameters in both the nAChR and CNGA2 systems.

We begin with the nAChR ion channel, whose allosteric gating parameter $\beta\epsilon$ has been exceedingly difficult to measure, since channel openings in the absence of ligand occur extremely infrequently. Instead of direct measurement, several groups measured the leakiness of nAChR channels with multiple pore mutations. The wild type channel parameter $\beta\epsilon^{(0)} \approx -14.2$ was then extrapolated by assuming that all of these pore mutations only affect the ϵ parameter and have energetically independent effects (i.e. if two mutations change ϵ by $\Delta\epsilon_1$ and $\Delta\epsilon_2$, respectively, then a channel with both mutations would change ϵ by $\Delta\epsilon_1 + \Delta\epsilon_2$).[14,15] Subsequently, dose-response curves were used to determine the values of the remaining thermodynamic parameters, namely, $K_O = 25 \times 10^{-9}$ M and $K_C = 150 \times 10^{-6}$ M.[5]

We first attempted to use these literature values directly to specify K_O and K_C for the entire class of nAChR mutants. However, using these values the $n = 4$ nAChR mutant cannot be well characterized for any value of $\beta\epsilon^{(4)}$ ($R^2 < 0.5$). Thus, we next examined the sensitivity of the measured $\beta\epsilon^{(0)} = -14.2$ parameter to see how well the full nAChR data set could be fit if this value was slightly altered. Fig S12A demonstrates that if $\epsilon^{(0)}$ is lowered by 4 k_BT, the family of nAChR mutants can once again be well characterized ($R^2 > 0.99$) by a single parameter set. In fact, as seen in Fig S12B, even a decrease of 2 k_BT in $\epsilon^{(0)}$ provides a reasonable fit ($R^2 = 0.98$) for the class of nAChR mutants. We note that 2 k_BT, roughly the energy of a hydrogen bond, is a very small energy, and this discrepancy may represent a source of error in the assumptions used to determine the $\beta\epsilon^{(0)} = -14.2$ value (e.g. that the effects of multiple channel pore mutations are additive and independent).

We now turn to how the MWC model compares to known literature values for the CNGA2 ion channel. In their paper, Wongsamitkul *et al.* reported single channel measurements for

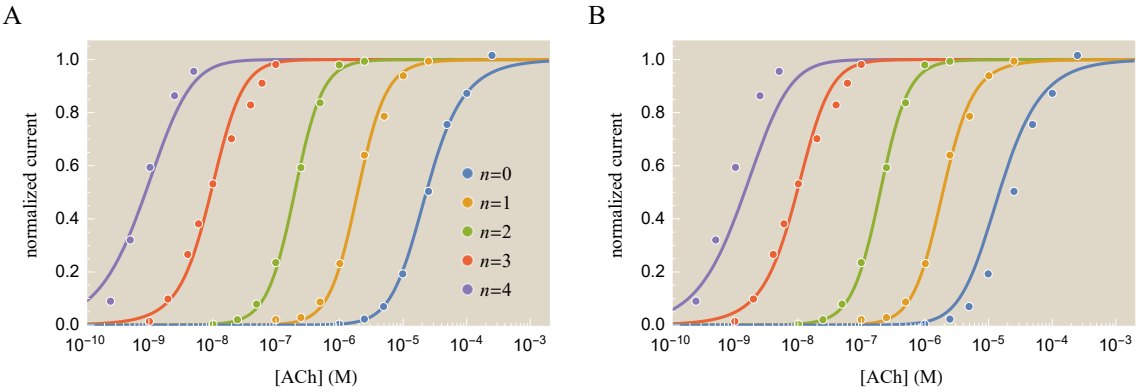

Figure S12: nAChR fits can be resolved by slightly perturbing the measured $\beta\epsilon$ value. (A) If the experimentally measured value of $\beta\epsilon^{(0)} = -14.2$ for wild type nAChR is decreased to $\beta\epsilon^{(0)} = -18$, we can characterize all of the nAChR mutants ($R^2 > 0.99$) using a single set of parameters given in Table S4. (B) Even the very modest change to $\beta\epsilon^{(0)} = -16$ enables us to fit most of the data set well ($R^2 = 0.98$).

the ratio of the open to closed state for the wild type ($n = 0$) channel, finding

$$\frac{[O]}{[C]} = 1.7 \times 10^{-5} = e^{\beta\epsilon} \tag{S51}$$

or equivalently $\beta\epsilon = -11$.[4] However, other sources have reported values as high as $\beta\epsilon = -6$ for this same ion channel.[16,17]

We find that the full spectrum of CNGA2 ion channel mutants can be fit to a single set of thermodynamic parameters (K_O, K_C, K_O^*, K_C^*, and $\beta\epsilon$) when $\beta\epsilon = -6$, as shown in Fig S13A (with $R^2 > 0.99$). Alternatively, using the value $\beta\epsilon = -9$ halfway between the experimental measurements yields markedly worse fits (with $R^2 = 0.97$), as shown in Fig S13B.

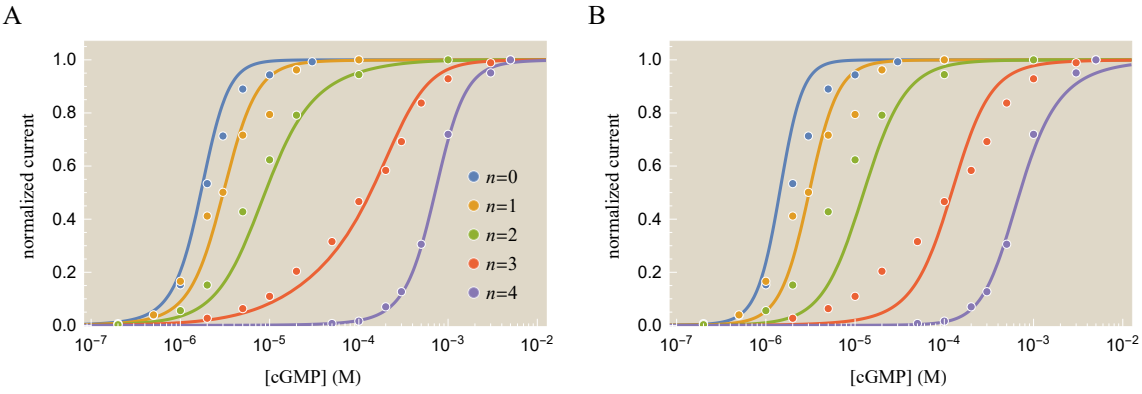

Figure S13: CNGA2 fits can also be resolved with slight changes to the measured $\beta\epsilon$ value. (A) Increasing the experimentally measured value of $\beta\epsilon = -11$ to $\beta\epsilon = -5$ permits us to recoup a single set of parameters ($R^2 > 0.99$) given by Table S5 for the entire class of mutants. (B) A more modest increase from $\beta\epsilon = -11$ to $\beta\epsilon = -8$ yields a poorer fit ($R^2 = 0.97$).

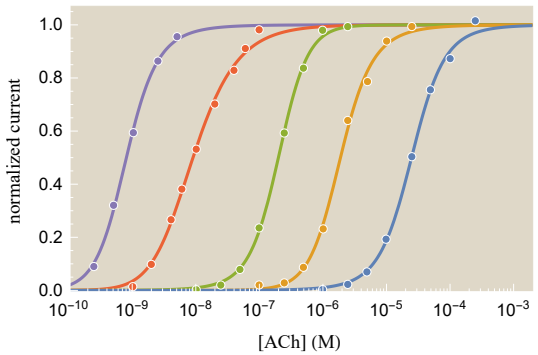

Figure S14: Extracting $[EC_{50}]$ and h from the nAChR data. The individual nAChR data sets can be fit to the MWC model in order to interpolate between the data points and extract the best possible $[EC_{50}]$ and h values. Note that each fit is very smooth around the midpoint where normalized current equals ½, which is the key region where both $[EC_{50}]$ and h are computed.

C.3 Fitting the nAChR Mutants with Non-Uniform K_O and K_C

In order to extract the $[EC_{50}]$ and effective Hill coefficient h of an nAChR ion channel from experimental measurements (Fig 3A), the individual data points must be connected in order to precisely infer where the normalized current reaches ½. This interpolation may be done in multiple ways, including connecting the data points with straight line segments or fitting the data to a sigmoidal function. The resulting $[EC_{50}]$ and h values can then be compared to the predictions in Fig 4 which were made while constraining all of the mutants to have the same K_O and K_C dissociation constants (which may have resulted in worse predictions for the characteristics of these mutants).

We chose to interpolate the nAChR data sets by fitting each mutant's data individually to the sigmoidal MWC response Eqs (1) and (2). Fig S14 shows how each data set is well fit by an individual MWC response, and that the behavior around the midpoint of each curve when normalized current equals to ½ is well aligned to the data, which gives us confidence that the corresponding $[EC_{50}]$ and h values that are extracted from these curves (see Fig 4C and D) will be precise. Note that the resulting best-fit parameters are not meaningful, as the sole purpose of this plot is to interpolate between the given data points in order to extract the best possible $[EC_{50}]$ and h values.

C.4 Degeneracy or "Sloppiness" within a Model

In this section, we examine the sloppiness inherent when fitting the nAChR and CNGA2 data (see Fig 10). This sloppiness demonstrates the possible trade-offs between best-fit parameter values that result in the nearly identical normalized current curves. Because of the startlingly simple relations between the parameters found in the nAChR case, we focus solely on that data set.

As seen in Fig 10A of the main text, the best-fit $\beta\epsilon^{(n)}$ parameters all depend upon the K_O parameter through the simple relationship $\beta\epsilon^{(n)} = 2\log(K_O) + \text{constant}$, while the best-fit value of K_C remains fixed for all K_O values. Fig S15 shows how these relationships can be

Table S4: Degenerate best-fit parameter sets for the nAChR mutants. Although the curves in Fig S15A and B look extremely similar and have the same goodness of fit as characterized by R^2, the latter has unreasonably small K_O and $\beta\epsilon^{(n)}$ values. This demonstrates the trade-offs between best-fit parameters embodied in Fig 10A. Fig S12A and B demonstrate the deviations in the parameter values if the wild type energy $\beta\epsilon^{(0)}$ was slightly increased, as is suggested by some literature values.

	K_O (M)	K_C (M)	$\beta\epsilon^{(0)}$	$\beta\epsilon^{(1)}$	$\beta\epsilon^{(2)}$	$\beta\epsilon^{(3)}$	$\beta\epsilon^{(4)}$	R^2
Fig S15A	0.8×10^{-9}	60×10^{-6}	-20.0	-15.4	-10.9	-5.0	-0.8	0.995
Fig S15B	4×10^{-27}	60×10^{-6}	-100.0	-95.4	-90.9	-84.8	-80.0	0.995
Fig S12A	2.1×10^{-9}	45×10^{-6}	-18.0	-13.5	-9.1	-3.3	2.0	0.995
Fig S12B	3.5×10^{-9}	15×10^{-6}	-16.0	-12.5	-8.2	-2.6	2.0	0.986

pushed to biologically unrealistic energy scales and still yield extremely similar curves.

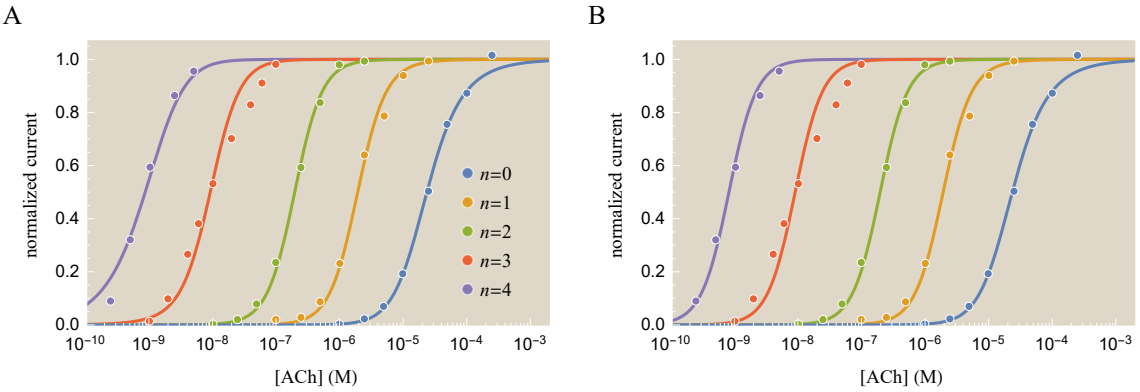

Figure S15: Different sets of parameters can yield nearly identical nAChR normalized current curves. (A) The nAChR data can be fit by fixing the wild type energy to either be $\beta\epsilon^{(0)} = -20$ and letting the remaining MWC parameters fit optimally. (B) The data can also be fit using $\beta\epsilon^{(0)} = -100$, which leads to equally good fit quality but results in energies that are far to small to be biologically feasible. The full set of parameters in both cases is shown in Table S4, and the fit parameters obey the relationship $e^{-\beta\epsilon/2}K_O = \text{constant}$ as seen in Fig 10A.

This suggests that K_C and $e^{-\beta\epsilon/2}K_O$ are the fundamental parameters combinations of the system. One means to confirm this result is to follow the framework in Ref. 12. We first rewrite the normalized current in terms of the log parameters

$$\beta\epsilon_O = \log\left(\frac{K_O}{1\,\text{M}}\right) \tag{S52}$$

$$\beta\epsilon_C = \log\left(\frac{K_C}{1\,\text{M}}\right). \tag{S53}$$

Next, we compute the Hessian matrix of normalized current whose components are given by

$$\boldsymbol{H}_{i,j} = \frac{\partial \text{normalized current}}{\partial x_i \partial x_j}, \tag{S54}$$

Table S5: Dependence of best-fit CNGA2 parameters with $\beta\epsilon$. Unlike in the nAChR system, the parameters in the CNGA2 system are much more tightly constrained (see Fig 10B). Even lowering $\beta\epsilon$ from -5 to -8 results in a poorer match between the theoretical predictions and the data. Literature values suggest that $\beta\epsilon$ may lie between -5 and -11.

	K_{O} (M)	K_{C} (M)	K_{O}^* (M)	K_{C}^* (M)	$\beta\epsilon$	R^2
Fig S13A	0.6×10^{-6}	40×10^{-6}	290×10^{-6}	200×10^{-3}	-5.0	0.993
Fig S13B	0.2×10^{-6}	60×10^{-6}	40×10^{-6}	800×10^{-6}	-8.0	0.976

which is a function of the logarithmic parameters

$$\boldsymbol{x} = \begin{pmatrix} \beta\epsilon \\ \beta\epsilon_O \\ \beta\epsilon_C \end{pmatrix}. \tag{S55}$$

We can evaluate the eigenvalues of the Hessian using the wild type MWC parameters ($\beta\epsilon = -23.7$, $\beta\epsilon_O = \log(0.1 \times 10^{-9})$, and $\beta\epsilon_C = \log(60 \times 10^{-6})$) throughout the range $c \in [10^{-6}, 3\times10^{-4}]$ M of ligand concentrations at which the wild type channel's dose-response curve was measured in Fig 3A. For example, at $c = 10^{-6}$ M, we find that the Hessian has the three eigenvalues $\{2 \times 10^{-2}, 9 \times 10^{-4}, 2 \times 10^{-7}\}$. This last eigenvalue has a corresponding eigenvector in the direction $(2, 1, 0)$. Because this last eigenvalue is significantly smaller than the other two, it indicates a direction in parameter space that the system can be perturbed without significantly modifying its response, which leads to sloppiness. Note that in the eigenvalue direction $(2, 1, 0)$, $e^{-\beta\epsilon/2}K_{\mathrm{O}}$ remains constant; by considering this parameter combination we effectively remove the sloppiness in the $\beta\epsilon$ and K_{O} parameters.

As yet another way to show how the parameter combinations K_{C} and $e^{-\beta\epsilon/2}K_{\mathrm{O}}$ may arise in our model, we rewrite $p_{\mathrm{open}}(c)$ from Eq (1) as

$$p_{\mathrm{open}}(c) = \frac{\left(e^{\beta\epsilon/2} + e^{\beta\epsilon/2}\frac{c}{K_{\mathrm{O}}}\right)^2}{\left(e^{\beta\epsilon/2} + e^{\beta\epsilon/2}\frac{c}{K_{\mathrm{O}}}\right)^2 + \left(1 + \frac{c}{K_{\mathrm{C}}}\right)^2}. \tag{S56}$$

The denominator can be approximated as $\left(e^{\beta\epsilon/2} + e^{\beta\epsilon/2}\frac{c}{K_{\mathrm{O}}}\right)^2 + \left(1 + \frac{c}{K_{\mathrm{C}}}\right)^2 \approx \left(e^{\beta\epsilon/2}\frac{c}{K_{\mathrm{O}}}\right)^2 + \left(1 + \frac{c}{K_{\mathrm{C}}}\right)^2$ as can be seen by considering the two possible regimes of the concentration: (1) when $c \gg K_{\mathrm{O}}$, $e^{\beta\epsilon/2} + e^{\beta\epsilon/2}\frac{c}{K_{\mathrm{O}}} \approx e^{\beta\epsilon/2}\frac{c}{K_{\mathrm{O}}}$ while (2) when $c \ll K_{\mathrm{O}}$ the left term $\left(e^{\beta\epsilon/2} + e^{\beta\epsilon/2}\frac{c}{K_{\mathrm{O}}}\right)^2$ will be negligible compared to the right term $\left(1 + \frac{c}{K_{\mathrm{C}}}\right)^2$ so that removing $e^{\beta\epsilon/2}$ from the left term will not noticeably affect the denominator. Thus, the formula for

$p_{\text{open}}(c)$ takes the form

$$p_{\text{open}}^{\text{approx}}(c) \approx \frac{\left(e^{\beta\epsilon/2}\frac{c}{K_{\text{O}}}\right)^2}{\left(e^{\beta\epsilon/2}\frac{c}{K_{\text{O}}}\right)^2 + \left(1+\frac{c}{K_{\text{C}}}\right)^2} \equiv \frac{\left(\frac{c}{\tilde{K}_{\text{O}}}\right)^2}{\left(\frac{c}{\tilde{K}_{\text{O}}}\right)^2 + \left(1+\frac{c}{K_{\text{C}}}\right)^2}. \tag{S57}$$

where we have introduced the effective dissociation constant $\tilde{K}_{\text{O}} = K_{\text{O}}e^{-\beta\epsilon/2}$. Thus, we once again find that only the parameter combinations K_{C} and $\tilde{K}_{\text{O}}$ will affect the nAChR response, whereas changing K_{O} and $e^{-\beta\epsilon}$ while keeping $\tilde{K}_{\text{O}}$ fixed will result in sloppiness.

Fig S16A demonstrates that $p_{\text{open}}(c)$ and $p_{\text{open}}^{\text{approx}}(c)$ lie on top of each other for the wild type nAChR values in Table S2. To show that this similarity was not mere happenstance, we fit the wild type data by constraining the gating energy $\beta\epsilon^{(0)}$ to the values shown on the x-axis of Fig S16B and letting the two other MWC parameters, K_{O} and K_{C}, find their optimal values. The resulting differences between $p_{\text{open}}(c)$ and $p_{\text{open}}^{\text{approx}}(c)$ will be very small for all ligand concentrations provided $\beta\epsilon^{(0)}$ is substantially negative, which is true for the entire class of nAChR mutants in Table S2.

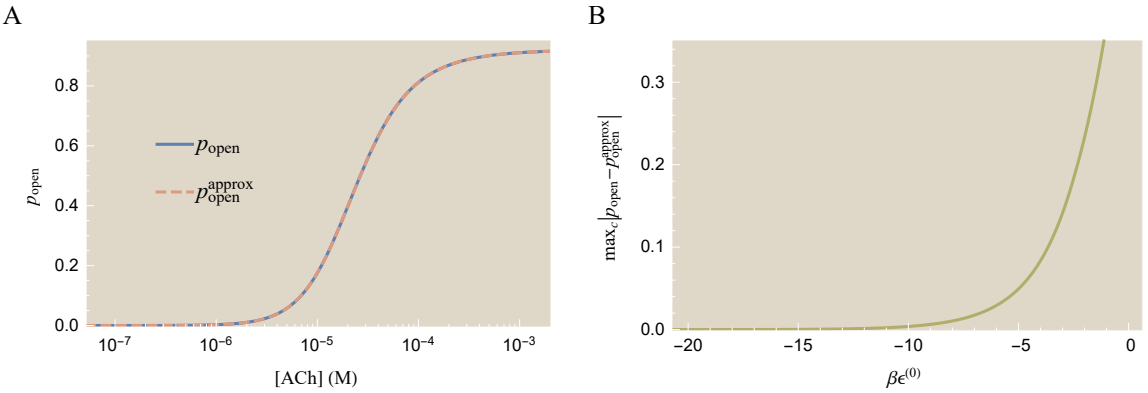

Figure S16: Exact versus approximate expressions of p_{open}. (A) A plot of the exact and approximate forms of p_{open} (see Eqs (S56) and (S57)) using the wild type parameters (K_{O}, K_{C}, and $\beta\epsilon^{(0)}$) from Table S2. (B) To check the accuracy of this approximation across many degenerate best-fit parameters, we fixed the wild type energy $\beta\epsilon^{(0)}$ to the value shown on the x-axis and fit the remaining MWC parameters (K_{O}, K_{C}) to the wild type data in Fig 3A. The maximum difference between p_{open} and $p_{\text{open}}^{\text{approx}}$ for any concentration c is extremely small when $\beta\epsilon^{(0)} \lesssim -5$, indicating that the approximate form strongly resembles the exact expression.

D Predicting the behavior of mutants using the MWC model

This section is intended to explore two related questions. First, experiments on nAChR ion channels with single point mutations in different subunits hint at the possibility that each mutation incurs the same energetic cost, as described by the MWC $\epsilon^{(n)}$ parameter (see Eq (20)). In D.1, we explore how well this hypothesis accords with the data and the predictive power that it grants the MWC model of nAChR. In D.2, we turn to the CNGA2 ion channels where the opposite hypothesis holds true, namely, that the gating energy ϵ is unaltered by subunit mutations while the remaining MWC parameters are impacted by these mutations. We again examine how a subset of the CNGA2 mutant data captures the behavior of the entire class of mutants.

D.1 nAChR

The wild type nAChR ion channel is characterized by the three MWC parameters K_{O}, K_{C}, and $\beta\epsilon^{(0)}$ (see Eqs (1) and (2)), all three of which can be fit from the wild type data set ($n = 0$ in Fig 3A). We further postulate that the L251S mutations will only change the allosteric energy $\beta\epsilon^{(0)}$, leaving the ligand binding affinities K_{O} and K_{C} unchanged.

The nAChR data suggests that each L251S mutation increases the gating equilibrium by $\Delta\epsilon$ per mutation, so that $\beta\epsilon^{(n)} = \beta\epsilon^{(0)} + n\Delta\epsilon$. We aim to find to what extent this hypothesis holds true. Specifically, we note that after the wild type data set fixes K_{O}, K_{C}, and $\beta\epsilon^{(0)}$, using one additional data set can fix $\Delta\epsilon$, enabling us to extrapolate the $\beta\epsilon^{(n)}$ values for the remaining mutants. For example, in Fig 9A of the main text, we used $\beta\epsilon^{(0)} = -23.7\ k_{\mathrm{B}}T$ and $\beta\epsilon^{(4)} = -4.0\ k_{\mathrm{B}}T$ to determine $\Delta\epsilon = -4.9\ k_{\mathrm{B}}T$, from which we determined $\beta\epsilon^{(1)} = -18.8\ k_{\mathrm{B}}T$, $\beta\epsilon^{(2)} = -13.9\ k_{\mathrm{B}}T$, and $\beta\epsilon^{(3)} = -8.9\ k_{\mathrm{B}}T$. The resulting predictions characterized the data sets for the $n = 1, 2, 3$ nAChR mutants remarkably well ($R^2 = 0.985$).

Note that this same procedure could work with any two nAChR data sets. For example, we could use the $n = 1$ mutant's data to determine the MWC parameters K_{O}, K_{C}, and $\beta\epsilon^{(1)}$, and then use the $n = 2$ data set to determine $\Delta\epsilon$ and extract the remaining $\beta\epsilon^{(n)}$ values. Fig S17 demonstrates the resulting predictions when all ten possible input pairs are used to predict the remaining three mutant dose-response curves. The corresponding best-fit parameters are given in Table S6. In each case, the two input curves used to extract the MWC parameters are shown as solid curves, while the three predicted responses are shown as dashed lines.

Most of the predictions do an especially good job of predicting the behavior of the intermediary $n = 1$, 2, and 3 mutants, while predictions for the two outer data sets $n = 0$ (wild type) and $n = 4$ are likely to be worse. This follows the general rule that interpolation - predicting values inside the domain of the training set - is more reliable than extrapolation. This suggests that when trying to make predictions for a similar family of mutants, it is most beneficial to acquire data for the extreme cases (i.e. the $n = 0$ and $n = 4$ data sets). In terms of the overall fit performance on the three unknown data sets in each of the ten plots, four of the fits have $R^2 > 0.9$ while four others have $0.9 > R^2 > 0.8$. This fit performance

is improved if three or four input data sets are used to predict the remaining dose-response curves, as shown in the supplementary *Mathematica* notebook.

Interestingly enough, when these predictions fail (most notably in Fig S17J), it occurs because the fitting captures the local details of (and noise in) the input data sets, which throws off the extrapolation to the remaining ion channel mutant. This concept is reminiscent of over-fitting in computer science. Indeed, it suggests that contrary to our intuition, using a more generalized model which has more degrees of freedom and is able to capture the tiny nuances of each individual data set even more precisely would do worse at predicting the global behavior of this class of mutants. In other words, having a coarse-grained model of the system with fewer parameters may provide a better opportunity to correctly predict protein behavior.

Table S6: nAChR parameter predictions from two input data sets. Data sets from the two plain text $\beta\epsilon^{(n)}$ columns (shown as solid lines in their corresponding figures) were used to determine the K_O and K_C dissociation constants for the entire class of mutants and to linearly extrapolate the energies (bold text) of the remaining mutants using Eq (20). R^2 indicates the goodness of fit for the three predicted curves (shown as dashed lines in the corresponding figures).

	K_O (M)	K_C (M)	$\beta\epsilon^{(0)}$	$\beta\epsilon^{(1)}$	$\beta\epsilon^{(2)}$	$\beta\epsilon^{(3)}$	$\beta\epsilon^{(4)}$	R^2
Fig S17A	0.3×10^{-9}	60×10^{-6}	−22.4	−17.8	**-13.2**	**-8.6**	**-4.1**	0.950
Fig S17B	20×10^{-9}	80×10^{-6}	−14.0	**-9.5**	−5.0	**-0.5**	**4.0**	0.868
Fig S17C	20×10^{-9}	80×10^{-6}	−13.7	**-8.6**	**-3.5**	1.6	**6.7**	0.839
Fig S17D	0.1×10^{-9}	80×10^{-6}	−23.8	**-18.8**	**-13.9**	**-8.9**	−4.0	0.985
Fig S17E	10×10^{-9}	10×10^{-6}	**-13.7**	−9.5	−5.4	**-1.2**	**2.9**	0.867
Fig S17F	20×10^{-9}	10×10^{-6}	**-13.9**	−8.8	**-3.7**	1.4	**6.6**	0.839
Fig S17G	0.1×10^{-9}	10×10^{-6}	**-23.8**	−18.8	**-13.9**	**-8.9**	−4.0	0.983
Fig S17H	20×10^{-9}	200×10^{-3}	**-17.0**	**-10.9**	−4.8	1.4	**7.5**	0.729
Fig S17I	0.1×10^{-9}	3×10^{-6}	**-25.0**	**-19.7**	−14.5	**-9.2**	−4.0	0.930
Fig S17J	0.1×10^{-9}	10×10^{-9}	**-20.7**	**-16.6**	**-12.5**	−8.4	−4.3	0.063

D.2 CNGA2

The wild type CNGA2 ion channel has 4 identical subunits with ligand affinity K_O in the open state and K_C in the closed state. The free energy difference between the closed and open states is given by ϵ. A mutation was introduced in the ligand binding site of any subunit, which results in new dissociation constants K_O^* in the open state and K_C^* in the closed state, but which will leave the free energy difference ϵ unchanged. Once all of the MWC parameters are known, a CNGA2 mutant with n mutated subunit and $4-n$ wild type subunits is fully described using Eq (15) with $m = 4$.

One conceptually simple route to resolving the MWC parameters is to first fix the wild type parameters K_O, K_C, and ϵ using the wild type data set ($n = 0$) and then fix the two mutant dissociation constants K_O^* and K_C^* from the $n = 4$ data set. From these parameters, the intermediate mutants $n = 1$, 2, and 3 would all follow from Eq (15). Yet, as in the case of nAChR, any two data sets could be used to fix the parameter values. In fact, in this system

all five thermodynamic parameters ($K_{\rm O}$, $K_{\rm C}$, $K_{\rm O}^*$, $K_{\rm C}^*$, and ϵ) could be fit using a *single* data set from one of the $n = 1$, 2, or 3 mutants, since the dose-response curve Eq (15) for such a mutant would contain all five parameters. Such fits are shown in the supplementary *Mathematica* notebook, but as expected the fits that utilize two input data sets do a much better job at predicting the remaining mutants.

Fig S18 shows the predictions (dashed lines) generated by fitting the MWC parameters to all possible input pairs (solid lines), with the best-fit parameters given in Table S7. As was found for the nAChR ion channels, the worst predictions resulted from data sets that are very close together (for example, when both input parameters came from $n = 2$, $n = 3$, or $n = 4$), which results in poor extrapolations for the remaining mutant data sets. Surprisingly, the prediction based on the $n = 0$ and $n = 4$ data set, which could be expected to be one of the best fits, was also poor. That said, the majority of the predictions were quite accurate ($R^2 > 0.96$), once again demonstrating the power of the simple statistical mechanical model we have employed.

Table S7: CNGA2 parameter predictions from two input data sets. Two data sets (shown as solid lines in the corresponding figures) were used to determine the thermodynamic parameters for the entire class of mutants. R^2 indicates the goodness of fit for the three predicted curves (shown as dashed lines in the corresponding figures).

	$K_{\rm O}$ (M)	$K_{\rm C}$ (M)	$K_{\rm O}^*$ (M)	$K_{\rm C}^*$ (M)	$\beta\epsilon$	R^2
Fig S18A	1.5×10^{-6}	35×10^{-6}	470×10^{-6}	70×10^{-3}	-3.6	0.983
Fig S18B	0.3×10^{-6}	15×10^{-6}	180×10^{-6}	3×10^{-3}	-5.5	0.962
Fig S18C	0.5×10^{-6}	6×10^{-6}	260×10^{-6}	5×10^{-3}	-4.6	0.962
Fig S18D	0.3×10^{-6}	5×10^{-6}	120×10^{-6}	2×10^{-3}	-6.5	0.857
Fig S18E	0.6×10^{-6}	20×10^{-6}	290×10^{-6}	2×10^{-3}	-4.3	0.982
Fig S18F	0.5×10^{-6}	5×10^{-6}	60×10^{-6}	170×10^{-6}	-4.6	0.978
Fig S18G	1×10^{-6}	30×10^{-6}	370×10^{-6}	4×10^{-3}	-3.9	0.990
Fig S18H	0.5×10^{-6}	4×10^{-6}	15×10^{-6}	140×10^{-3}	-4.1	0.883
Fig S18I	0.1×10^{-6}	3×10^{-6}	20×10^{-6}	20×10^{-6}	-10.2	0.640
Fig S18J	0.5×10^{-6}	4×10^{-6}	3×10^{-6}	140×10^{-3}	-4.6	0.713

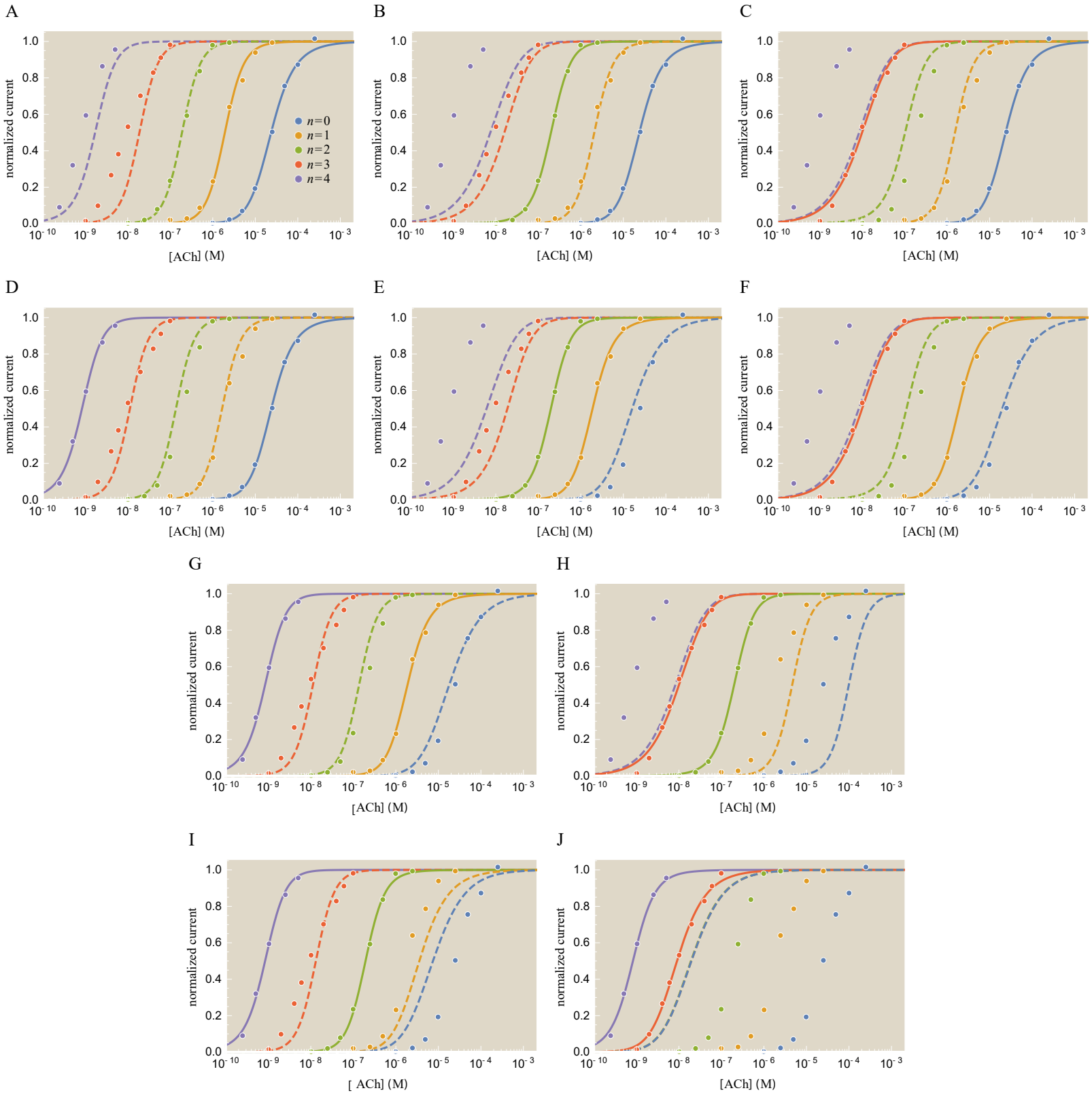

Figure S17: Predicting nAChR mutants using different training sets. The MWC parameters for the entire class of nAChR mutants can be fit from two data sets (solid lines). Using these parameters, the dose-response curves of the remaining three mutants can be predicted (dashed lines) without any further fitting. The best-fit parameters are listed in Table S6.

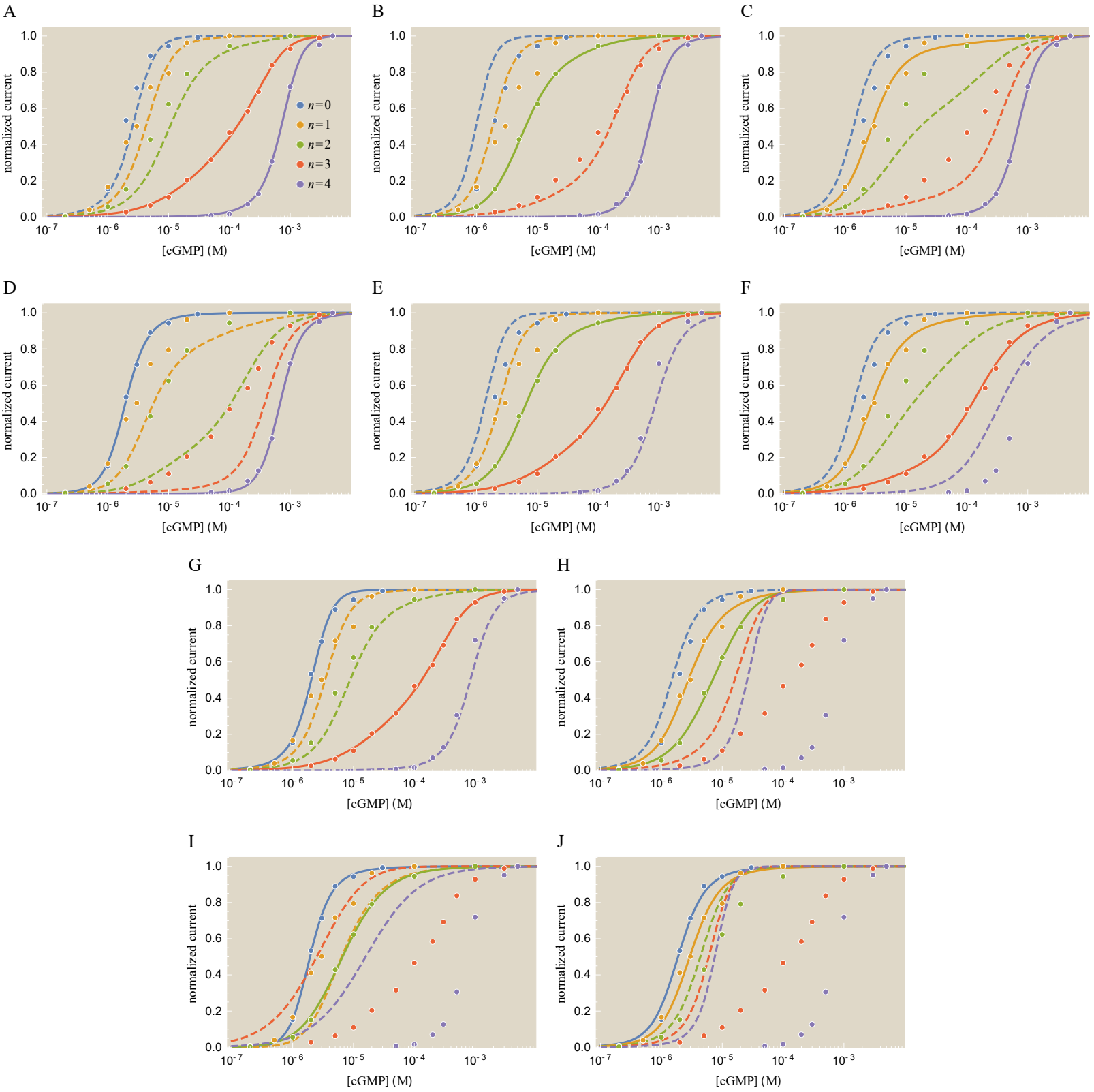

Figure S18: Predicting CNGA2 mutants using different training sets. As was found for nAChR, two data sets (solid lines) are sufficient to extract the MWC parameters for the whole class of CNGA2 mutants, which can then be used to extrapolate the responses of the remaining mutants (dashed lines). The best-fit parameters are listed in Table S7.

References

(1) Mirzaev, I.; Gunawardena, J. Laplacian Dynamics on General Graphs. *Bull. Math. Biol.* **2013**, *75*, 2118–2149.

(2) Unwin, N. Acetylcholine Receptor Channel Imaged in the Open State. *Nature* **1995**, *373*, 37–43.

(3) Labarca, C.; Nowak, M. W.; Zhang, H.; Tang, L.; Deshpande, P.; Lester, H. A. Channel Gating Governed Symmetrically by Conserved Leucine Residues in the M2 Domain of Nicotinic Receptors. *Nature* **1995**, *376*, 514–516.

(4) Wongsamitkul, N.; Nache, V.; Eick, T.; Hummert, S.; Schulz, E.; Schmauder, R.; Schirmeyer, J.; Zimmer, T.; Benndorf, K. Quantifying the Cooperative Subunit Action in a Multimeric Membrane Receptor. *Sci. Rep.* **2016**, *6*, 20974.

(5) Auerbach, A. Thinking in Cycles: MWC is a Good Model for Acetylcholine Receptor-Channels. *J. Physiol.* **2012**, *590*, 93–8.

(6) Gunawardena, J. A Linear Framework for Time-Scale Separation in Nonlinear Biochemical Systems. *PLoS ONE* **2012**, *7*, e36321.

(7) Krashia, P.; Moroni, M.; Broadbent, S.; Hofmann, G.; Kracun, S.; Beato, M.; Groot-Kormelink, P. J.; Sivilotti, L. G. Human $\alpha 3\beta 4$ Neuronal Nicotinic Receptors Show Different Stoichiometry if they are Expressed in Xenopus Oocytes or Mammalian HEK293 Cells. *PLoS ONE* **2010**, *5*, e13611.

(8) George, A. A.; Lucero, L. M.; Damaj, M. I.; Lukas, R. J.; Chen, X.; Whiteaker, P. Function of Human $\alpha 3\beta 4\alpha 5$ Nicotinic Acetylcholine Receptors is Reduced by the $\alpha 5$(D398N) Variant. *J. Biol. Chem.* **2012**, *287*, 25151–25162.

(9) Filatov, G. N.; White, M. M. The Role of Conserved Leucines in the M2 Domain of the Acetylcholine Receptor in Channel Gating. *Mol. Pharmacol.* **1995**, *48*, 379–84.

(10) Martins, B. M. C.; Swain, P. S. Trade-Offs and Constraints in Allosteric Sensing. *PLoS Comput. Biol.* **2011**, *7*, 1–13.

(11) Marzen, S.; Garcia, H. G.; Phillips, R. Statistical Mechanics of Monod-Wyman-Changeux (MWC) Models. *J. Mol. Biol.* **2013**, *425*, 1433–60.

(12) Transtrum, M. K.; Machta, B. B.; Brown, K. S.; Daniels, B. C.; Myers, C. R.; Sethna, J. P. Perspective: Sloppiness and Emergent Theories in Physics, Biology, and Beyond. *J. Chem. Phys.* **2015**, *143*, 010901.

(13) Milo, R.; Hou, J. H.; Springer, M.; Brenner, M. P.; Kirschner, M. W. The Relationship Between Evolutionary and Physiological Variation in Hemoglobin. *Proc. Natl. Acad. Sci. U. S. A.* **2007**, *104*, 16998–17003.

(14) Nayak, T. K.; Purohit, P. G.; Auerbach, A. The Intrinsic Energy of the Gating Isomerization of a Neuromuscular Acetylcholine Receptor Channel. *J. Gen. Physiol.* **2012**, *139*, 349–58.

(15) Jackson, M. B. Kinetics of Unliganded Acetylcholine Receptor Channel Gating. *Biophys. J.* **1986**, *49*, 663–72.

(16) Nache, V.; Schulz, E.; Zimmer, T.; Kusch, J.; Biskup, C.; Koopmann, R.; Hagen, V.; Benndorf, K. Activation of Olfactory-Type Cyclic Nucleotide-Gated Channels is Highly Cooperative. *J. Physiol.* **2005**, *569*, 91–102.

(17) Tibbs, G. R.; Goulding, E. H.; Siegelbaum, S. A. Allosteric Activation and Tuning of Ligand Efficacy in Cyclic-Nucleotide-Gated Channels. *Nature* **1997**, *386*, 612–615.